Title

Performance comparison of r2SCAN and SCAN metaGGA density functionals for solid materials via an automated, high-throughput computational workflow

Journal

Physical Review Materials, 6(1)

ISSN

2476-0455

Authors

Kingsbury, Ryan

Gupta, Ayush S

Bartel, Christopher J

et al.

Publication Date

2022

DOI

10.1103/physrevmaterials.6.013801

Performance comparison of r^{2}SCAN and SCAN metaGGA density functionals for solid materials via an automated, high-throughput computational workflow

Ryan Kingsbury,[1,2] Ayush Gupta,[1,3] Christopher J. Bartel,[1] Jason M. Munro,[3] Shyam Dwaraknath,[3] Matthew Horton,[3] and Kristin A. Persson[1,4,*]

[1]*Department of Materials Science and Engineering, University of California Berkeley, Berkeley, CA 94720*
[2]*Energy Technologies Area Lawrence Berkeley National Laboratory, Berkeley, CA 94720*
[3]*Materials Science Division Lawrence Berkeley National Laboratory, Berkeley, CA 94720*
[4]*Molecular Foundry Lawrence Berkeley National Laboratory, Berkeley, CA 94720*

(Dated: September 13, 2021)

Computational materials discovery efforts utilize hundreds or thousands of density functional theory (DFT) calculations to predict material properties. Historically, such efforts have performed calculations at the generalized gradient approximation (GGA) level of theory due to its efficient compromise between accuracy and computational reliability. However, high-throughput calculations at the higher metaGGA level of theory are becoming feasible. The Strongly Constrained and Appropriately Normed (SCAN) metaGGA functional offers superior accuracy to GGA across much of chemical space, making it appealing as a general-purpose metaGGA functional, but it suffers from numerical instabilities that impede it's use in high-throughput workflows. The recently-developed r^{2}SCAN metaGGA functional promises accuracy similar to SCAN in addition to more robust numerical performance. However, its performance compared to SCAN has yet to be evaluated over a large group of solid materials. In this work, we compared r^{2}SCAN and SCAN predictions for key properties of approximately 6,000 solid materials using a newly-developed high-throughput computational workflow. We find that r^{2}SCAN predicts formation energies more accurately than SCAN and PBEsol for both strongly- and weakly-bound materials and that r^{2}SCAN predicts systematically larger lattice constants than SCAN. We also find that r^{2}SCAN requires modestly fewer computational resources than SCAN and offers significantly more reliable convergence. Thus, our large-scale benchmark confirms that r^{2}SCAN has delivered on its promises of numerical efficiency and accuracy, making it a preferred choice for high-throughput metaGGA calculations.

I. INTRODUCTION

Density functional theory (DFT) has emerged as the most widely-used computational method for predicting material properties in recent decades [1]. Hundreds of thousands of DFT calculations now populate materials databases such as the Materials Project [2], NOMAD [3], or OQMD [4, 5], laying the foundation for a new era of data-driven materials discovery [6].

The vast majority of these calculations employ the Perdew-Burke-Ernzerhof (PBE) [7] generalized gradient approximation (GGA) [8] functional, due to its popularity among researchers and its efficient compromise between high accuracy and high performance across a wide variety of chemistries and properties. However, as a semi-local GGA functional, PBE and its variants such as PBEsol [9] have well-documented and systematic errors related to electron self-interaction [1, 10] and fail to capture medium- and long-range dispersion [1, 11]. These errors compromise their predictive accuracy for many properties of interest. Specifically, PBE systematically under-predicts the magnitude of formation energies (i.e., under-binds) [12], slightly over-predicts lattice parameters [12, 13], and severely under-predicts semiconductor bandgaps [12, 14, 15]. In principle, higher levels of theory such as metaGGA DFT functionals can capture medium-range dispersion interactions and should exhibit smaller self-interaction errors than GGA functionals such as PBE [10]. However, metaGGA functionals have historically been either too specific to selected properties or chemistries and/or too computationally demanding to be feasible for high-throughput calculations across the entire periodic table.

The challenge of generality was addressed by Sun and co-workers via development of the Strongly Constrained and Appropriately Normed (SCAN) [16] functional. This non-empirical metaGGA functional has been shown to be substantially more accurate than PBE for predicting lattice constants and ground-state structures of solids [13, 17–20], and modestly more accurate for semiconductor bandgaps [12, 15]. SCAN predicts formation energies more accurately than PBE for strongly-bound compounds, but less accurately than PBE for weakly-bound compounds (e.g., intermetallics) [12]. Researchers have also noted that SCAN underpredicts some lattice parameters compared to experiment [12] and identified shortcomings in SCAN's predictions of the magnetic moments of ferromagnetic systems [21, 22], the ground-state poly-

* kapersson@lbl.gov

morphs of selected binary compounds [13], and the elastic constants of water ice [23]. Nevertheless, the generally superior accuracy of SCAN compared to PBE across many chemical systems and properties makes it appealing as a general-purpose functional for solids. However, it has a higher computational cost than PBE (by a factor of about 5 [12, 24]), and suffers from numerical instability. This numerical instability in particular makes it impractical to reliably and efficiently perform automated, high-throughput calculations with SCAN.

To mitigate the computational challenge, Furness and co-workers recently introduced r^{2}SCAN [25], a modification of the original SCAN functional with substantially improved numerical stability, allowing calculations to converge much more reliably than in the original SCAN functional. This improved stability is achieved by relaxing one of the 17 theoretical constraints satisfied by the original SCAN functional (specifically, the fourth order gradient expansion constraint for exchange GE4X [25]), resulting in a smoother potential energy surface free of discontinuities. r^{2}SCAN was shown to largely preserve the accuracy of SCAN when benchmarked against several hundred molecular properties and 20 solid lattice constants [25]. Hence, it would appear that the arrival of r^{2}SCAN has at last created a general-purpose, numerically-robust metaGGA functional. However, its accuracy compared to SCAN has yet to be demonstrated for a large group of solid materials.

To further promote progress towards high-throughput metaGGA DFT calculations for solids, in this work we compare the formation energies, cell volumes, and electronic structures of approximately 6,000 solid materials calculated in r^{2}SCAN and SCAN by means of an automated, high-throughput workflow. We show that r^{2}SCAN achieves comparable or even improved accuracy compared to SCAN and reaches convergence much more reliably for this large and diverse set of calculations.

II. METHODOLOGY

A. Automated workflow for metaGGA calculations

DFT calculations were carried out using a two-step workflow comprising an initial GGA structure optimization followed by a structure optimization with the SCAN [16] or r^{2}SCAN [25] metaGGA functionals, coupled with automatic error correction logic (see Figure 1). The purpose of the initial GGA structure optimization was to generate an initial guess of the structure and charge density at lower computational cost, thereby speeding up the subsequent metaGGA calculation. Performing two optimizations in series also makes the calculation more robust to changes in the size or shape of the unit cell, as elaborated further in Appendix A. SCAN calculations used PBE [7] for the initial GGA optimization, while r^{2}SCAN calculations employed the PBEsol [9] functional, which is a variant of PBE tuned to predict solid lattice constants with greater accuracy. Since the purpose of the initial GGA calculation is simply to accelerate the metaGGA optimization, the final metaGGA result should not be particularly sensitive to the choice of GGA functional.

We employed the Vienna ab initio Simulation Package (VASP) [26, 27], version 6.1.1 with custom patches for r^{2}SCAN, in conjunction with projected augmented wave (PAW) pseudopotentials [28] and a plane-wave energy cutoff of 680 eV. Note that r^{2}SCAN is officially available in VASP as of version 6.2. k-point grids were generated automatically by VASP using KSPACING values ranging from 0.22 to 0.44 Å^{-1}, which were determined from the GGA-estimated bandgap of each material based on the work of Wisesa et al. [29]. Plane-wave energy cutoff and k-point density settings were selected such that formation energies converged within approximately 1 meV/atom for a benchmark set of 21 materials (listed in Appendix A) and were selected to be conservatively high. All calculations used pseudopotentials from the "PBE PAW datasets version 54" set released in September 2015; a list of the specific POTCAR symbols used for each element is provided in Appendix I. Although these pseudopotentials were developed for use with the PBE functional, their use with SCAN is common practice because no SCAN-specific pseudopotentials are available for use in VASP. Additional details related to development of our computational workflow are provided in Appendix A.

B. Selection of materials

The dataset we analyze below includes 6,307 distinct materials, comprising 412 elements, 5,297 binary materials, and 598 ternary materials whose elemental compositions cover the majority of the periodic table (see Figure C.1). We first screened the Materials Project Database [30] for materials that were within 20 meV of the convex energy hull and had 20 or fewer sites, resulting in a set of approximately 45,000 materials. We retrieved PBE-relaxed structures for each of these from the Materials Project REST API [30], which we used as starting structures in our computational workflow. We initially sought to compute all 45,000 materials using SCAN; however we were able to complete only approximately 8,000 due to convergence problems and computational constraints. Using r^{2}SCAN, we were able to complete approximately 25,000 materials with the available computational resources, and we did not encounter significant problems with convergence (as discussed further below). Among these SCAN and r^{2}SCAN calculations, there are 6,307 materials (including 5,895 non-elemental solids) for which both SCAN and r^{2}SCAN calculations were completed. We use this set of materials to compare the properties predicted by the two functionals. We note that the ≈ 1,700 materials for which we completed SCAN but not r^{2}SCAN calculations do not indicate cases where r^{2}SCAN failed to converge. Rather, after complet-

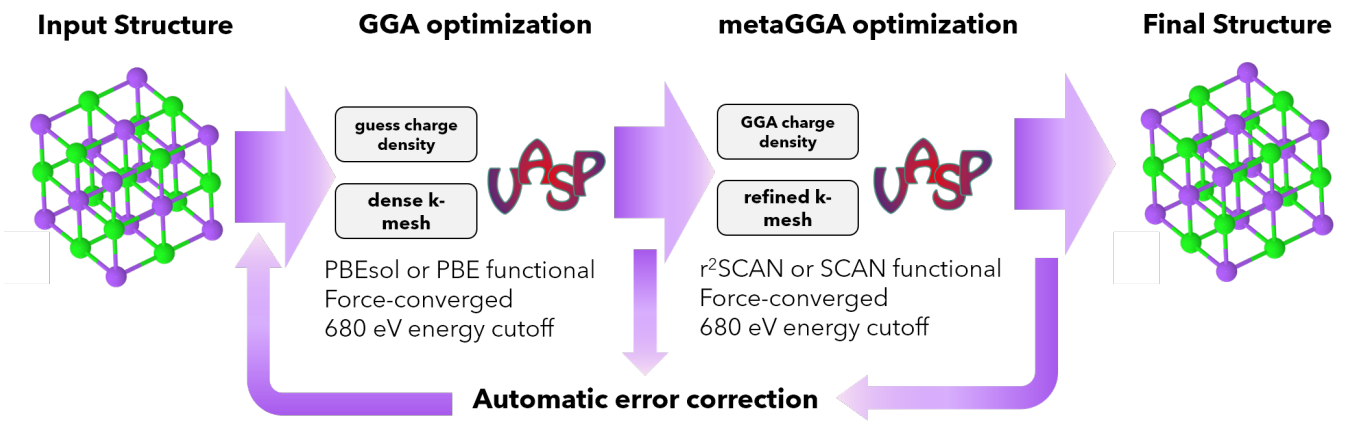

FIG. 1. Automated workflow for metaGGA calculations. The input structure is used to construct an initial guess of the charge density for the GGA optimization using a GGA functional. A high k-point density is used in this step. The output charge density from the GGA optimization is used as the initial guess in the subsequent metaGGA optimization using either r^{2}SCAN or SCAN. The bandgap estimated from the GGA calculation is used to refine the k-point density for the metaGGA optimization, where metals have the highest k-point density and semiconductors or nonmetals have lower k-point density. Automated error correction routines adjust settings and restart calculations that fail for well-defined reasons, improving reliability.

ing our SCAN calculations we chose to prioritize calculations slightly differently for r^{2}SCAN, and hence some materials originally completed in SCAN were not attempted in r^{2}SCAN.

III. RESULTS AND DISCUSSION

A. Relative comparison of r^{2}SCAN vs SCAN

1. *Formation Energy*

Computed formation energies predicted by r^{2}SCAN and SCAN are summarized in Figure 2a. In an extensive benchmark of the original SCAN functional, Isaacs and Wolverton [12] observed that SCAN formation energies were somewhat more accurate for strongly-bound compared to weakly-bound materials, where 'strongly-bound' materials are those with formation energies ≤ -1 eV/atom and 'weakly-bound' materials are those with formation energies between 0 and -1 eV/atom. We adopt the same categories here to facilitate comparison with this prior work. By this definition, our data contains 1,428 and 4,317 strongly- and weakly-bound materials, respectively. We exclude any materials containing U, Np, or Pu (150 materials), because many exhibited exceptionally large differences in formation energy between the two functionals. For these cases, we found that r^{2}SCAN-predicted formation energies were substantially more accurate than SCAN-predicted energies compared to experiment. However, since these calculations were performed without spin-orbit coupling, the results must be interpreted with caution and we do not consider them in detail here. Further discussion is provided in Appendix D.

Overall, r^{2}SCAN and SCAN predicted similar formation energies for most materials within both the strongly- and weakly-bound categories, as indicated by the fact that the median difference in formation energy was only -5 meV/atom. Nevertheless, there were substantial differences for many materials. For 95% of strongly-bound materials, $\Delta H_f^{\text{r}^2\text{SCAN}}$ differed from ΔH_f^{SCAN} by ≈ -135 to $+170$ meV/atom, while for weakly-bound materials, the 95th-percentile difference in formation energy was ≈ -105 to $+115$ meV/atom. Although the absolute differences in formation energy were similar for strongly- and weakly-bound materials, in *relative* terms they are much more significant for weakly-bound materials, since the magnitude of ΔH_f for weakly-bound materials is smaller by definition. Reassuringly, we find that in spite of these apparently large relative differences in predicted ΔH_f for weakly-bound materials, r^{2}SCAN has a lower average error compared to experiment by every measure(see Section III B 1).

In Appendix G we analyze how differences in r^{2}SCAN and SCAN formation energies relate to specific chemistries. Among strongly- and weakly-bound materials, the largest positive differences (i.e., materials for which $\Delta H_f^{\text{r}^2\text{SCAN}}$ was less negative than ΔH_f^{SCAN}) were materials containing Pt or Au, while Co, Ni, Rh, and Pd-containing materials also tended to have less negative $\Delta H_f^{\text{r}^2\text{SCAN}}$. On the other hand, the largest negative differences in formation energy were observed for Cs, Pa, Br and Bi-containing materials. It is unclear why the largest differences in formation energy are associated with materials containing these particular elements. For the negative differences, a possible explanation may be that intermediate van der Waals interactions in the elemental Cs, Pa, Br and Bi phases are less captured by r^{2}SCAN than SCAN [31]. In general, however, differences in el-

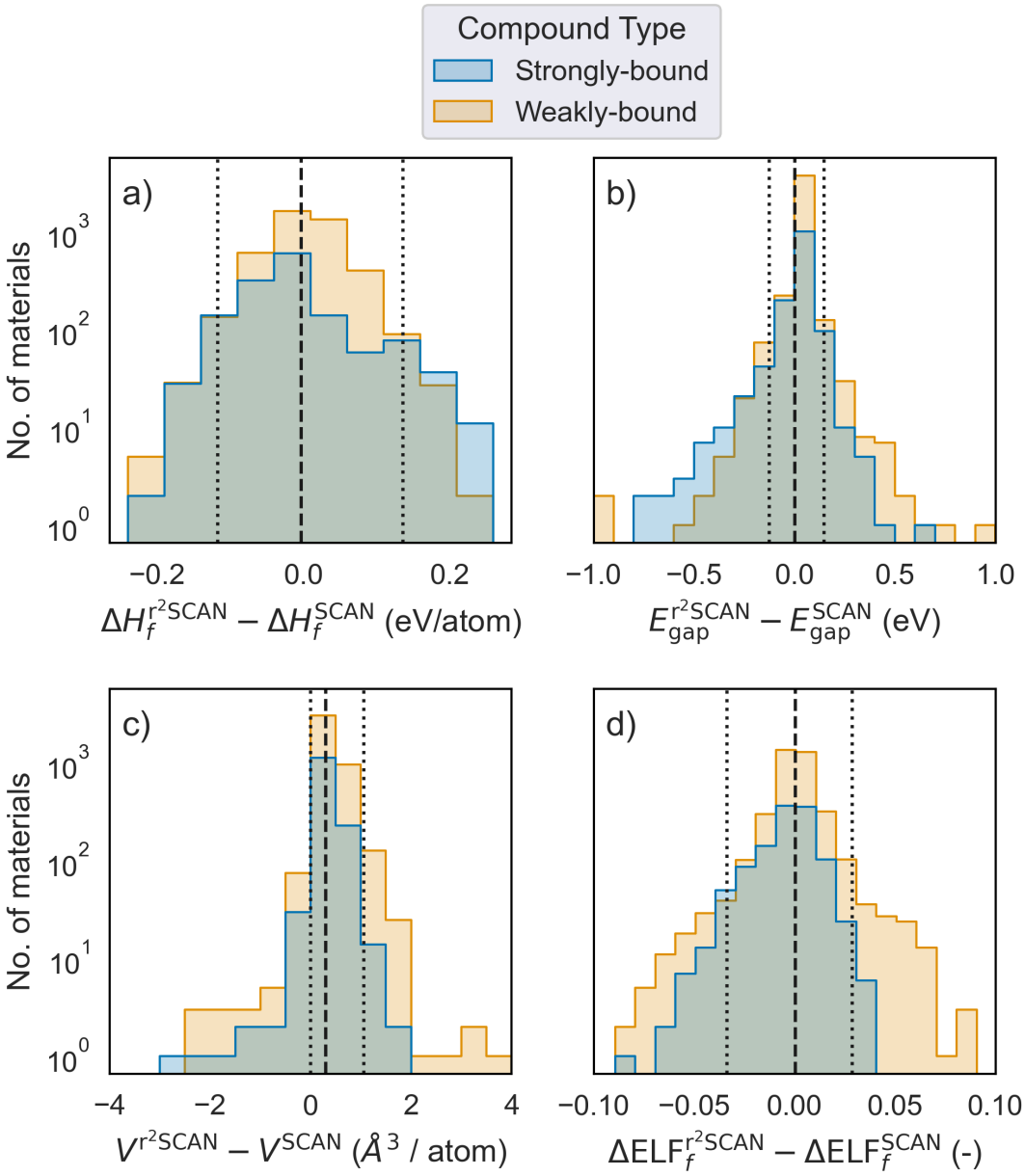

FIG. 2. Changes in a) formation energy, b) bandgap, c) cell volume, and d) formation electron localization function (ΔELF_f; see Appendix E) when computed in r^{2}SCAN vs SCAN. Note that the y axis is logarithmic. Dashed and dotted vertical lines represent the median differences and two-sided 95th percentile differences, respectively, across both material categories.

emental energies do not explain our observations. For pure elements, the difference in electronic energy between r^{2}SCAN and SCAN grows systematically larger with the atomic number (Figure F.1), hence one might expect materials containing heavier elements to exhibit the largest differences in formation energy. This is not what we observed: formation energies of materials show no such systematic trend (Figure G.1 and G.2). Since the formation energy of a material is calculated by subtracting the energies of elemental references from that of the material, it would appear that the sometimes substantial differences in formation energy predicted by r^{2}SCAN and SCAN are attributable to different energies of the materials rather than the elemental references.

2. *Bandgaps*

GGA DFT functionals are known to systematically and significantly underestimate bandgaps, and this shortcoming is only slightly mitigated by SCAN [12]. Nevertheless, it is instructive to examine whether r^{2}SCAN-predicted bandgaps differ substantially from those predicted by SCAN (Figure 2b). For strongly and weakly

bound materials, r^{2}SCAN bandgaps were within ±0.15 eV of SCAN-predicted bandgaps for 95% of materials studied. r^{2}SCAN was slightly more likely to predict a smaller bandgap than SCAN for strongly-bound materials and a larger bandgap than SCAN for weakly-bound materials.

Qualitative agreement between the r^{2}SCAN and SCAN predicted metallic character of materials is arguably more relevant than the quantitative bandgap predictions. Out of 5,895 materials for which we computed bandgaps, there were 73 cases (≈ 1%, listed in Table B.1) in which r^{2}SCAN predicted metallic character (zero bandgap) when SCAN predicted non-metallic character or vice versa. In six of these cases, the predictions differed by $\gtrsim$ 1 eV. Manual inspection of the density of states (DOS; see Appendix B) for the materials with the largest discrepancies indicates that they represent edge cases in which the band occupancies are particularly sensitive to the exchange energy. For example, the material Sb_2F_{13}, was a notable outlier where r^{2}SCAN predicted a metallic material rather than the large-gap insulator predicted by SCAN, due to a small amount of ferromagnetism in the r^{2}SCAN case shifting the Fermi level into the valence band. Thus, the subtle differences in construction between r^{2}SCAN and SCAN can occasionally result in large differences in predicted bandgaps. However, this example represents a fictitious, unphysical material, since the originating crystal structure file was found to have omitted hydrogens when compared against the original publication. We emphasize, that we observed these large discrepancies in only ≈ 0.1% of materials in our dataset, and that they may be partially attributable to recently-identified changes in the way VASP computes the Fermi level.

3. Lattice Volumes

r^{2}SCAN systematically predicted larger lattice volumes for many materials than SCAN, and this systematic difference was observed to a similar extent across both material categories (Figure 2c). Specifically, the median volumes per atom predicted by r^{2}SCAN were 1.4% and 1.8%, (0.2 - 0.3 Å^3/atom) larger than the SCAN predicted volumes for strongly-bound and weakly-bound materials, respectively. The systematically larger lattice volumes predicted by r^{2}SCAN compared to SCAN may be fortuitous, since SCAN was previously shown to under-predict experimental lattice volumes by an average of 0.11 Å^3/atom [12]. We will examine the accuracy of SCAN and r^{2}SCAN lattice volumes compared to experiment in a later section.

4. Electron Localization

To evaluate the consistency between r^{2}SCAN and SCAN in a more general way, we next present differences in the electronic structure predicted by the two functionals. Both r^{2}SCAN and SCAN incorporate information about the kinetic energy density into their calculation of the exchange and correlation energies by means of the iso-orbital indicator $\alpha = \frac{\tau-\tau_W}{\tau_{unif}}$ or $\bar{\alpha} = \frac{\tau-\tau_W}{\tau_{unif}+\eta\tau_W}$ for SCAN and r^{2}SCAN, respectively, where τ is the positive kinetic energy density, τ_W and τ_{unif} are the limiting kinetic energies of a single orbital and uniform electron gas, respectively and η=0.001 is a regularization parameter [10, 25]. The calculated value of the exchange and correlation energies depends on the value of the iso-orbital indicator, and hence on the bonding regime (e.g. localized/covalent or delocalized/metallic). This ability to adjust for different local electronic environments is a major reason for the superior accuracy of r^{2}SCAN and SCAN compared to GGA [12], and also explains why SCAN requires much smaller Hubbard U values than GGA functionals to accurately predict formation energies of transition metal oxides [32].

r^{2}SCAN differs from SCAN primarily in that 1) it uses $\bar{\alpha}$ instead of α as the iso-orbital indicator (see definitions above) and 2) it uses a different 'switching function' to adjust the value of the exchange-correlation enhancement factor, F_{xc}, for different values of $\bar{\alpha}$ [25]. The iso-orbital indicator is closely related to the electron localization function (ELF), which is equal to $(1+\alpha^2)^{-1}$ [16, 25] and ranges from 0 to 1, where a value of 0.5 corresponds to an electron gas and 1 corresponds to highly localized (covalent) bonding [33]. Since both α and $\bar{\alpha}$ and hence the value of F_{xc} are directly related to ELF, in Figure 2d we present the difference in 'formation ELF', ΔELF_f, predicted by r^{2}SCAN and SCAN. ΔELF_f is calculated by analogy to the formation energy (see Appendix E1), and represents the degree to which the average amount of electron localization around each atom in a material differs from that in the corresponding elemental references. By construction, the formation ELF must fall between 0 and 1. However, because high electron localization occurs only in a relatively small fraction of the volume occupied by a crystal (e.g., near the nuclei or along a covalent bond), average values for an entire atomic basin are typically small. An example illustrating the local value of ELF in a crystal structure is provided in Appendix E. In our dataset, the median values of ΔELF_f were 0.034 and 0.036 (dimensionless) for r^{2}SCAN and SCAN, respectively. These values are 10-20% larger than the median ΔELF_f calculated by PBEsol (0.030), indicating that the two metaGGA functionals predict larger changes in electronic structure during compound formation than GGA.

Figure 2d shows that broadly speaking, ΔELF_f values predicted by r^{2}SCAN and SCAN are similar for both categories of materials (as indicated by the differences being centered around 0). There is a slight skew towards r^{2}SCAN predicting smaller ΔELF_f (i.e., less change in localization between elements and compounds) than SCAN, with differences of −0.033 to +0.028 defining the 95th percentile of all materials. However in relative

terms (i.e., $\left|\frac{\Delta\mathrm{ELF}_f^{\mathrm{r^2SCAN}}-\Delta\mathrm{ELF}_f^{\mathrm{SCAN}}}{\Delta\mathrm{ELF}_f^{\mathrm{SCAN}}}\right|$) these changes were quite large, with a median relative change of 16% and a 95th percentile relative change of 82%. Hence, while r^{2}SCAN and SCAN predict similar $\Delta\mathrm{ELF}_f$ in aggregate, subtle absolute differences in their respective prediction of ELF may result in large relative changes for specific materials.

By definition, the difference in DFT energy between the two functionals when evaluated on the same density (and Kohn-Sham orbitals) is equal to the difference in their exchange and correlation energy, which is a complex function of not only the ELF, but also the density, density gradient, and kinetic energy density [10, 25] which are themselves products of previous self-consistent iterations. Hence, it is difficult to relate changes in $\Delta\mathrm{ELF}_f$ directly to changes in DFT or formation energy. Figure 2a suggests that the large relative shifts in $\Delta\mathrm{ELF}_f$ that we observe between r^{2}SCAN and SCAN do not lead to commensurately large shifts in ΔH_f. For comparison, the median and 95th percentile relative changes in the electronic energy (i.e., the DFT energy) from SCAN to r^{2}SCAN were 26% and 32%, respectively, while the median and 95th percentile changes in ΔH_f were 6.5% and 54%. Nevertheless, Figure 2d shows that differences in $\Delta\mathrm{ELF}_f$ tended to be larger for weakly-bound materials compared to strongly-bound materials, and this fact could be related to the larger relative changes in formation energy that we observed for weakly-bound materials (see above).

B. Experimental benchmarks

1. Formation Energy

Having examined how material properties predicted by r^{2}SCAN differ from those of SCAN, we now turn our attention to how accurately r^{2}SCAN and SCAN predict experimental formation energies, volumes, and bandgaps. Predictions by the PBEsol GGA functional [9], executed with the same settings as the first step of the automated workflow (see Section II A) are shown as an additional point of comparison. We note that since experimental benchmarking was not the primary objective of this work, the materials we evaluate in this section are dictated primarily by the calculations we generated rather than through deliberate selection. Complementary efforts are underway by other research groups [31] to benchmark r^{2}SCAN against experimental data using carefully-curated sets of materials presented in previous studies [12, 17].

Figure 3a shows the mean absolute error (MAE) in formation energy for 986 materials. Experimental energies for these materials were obtained from the `expt_formation_energy_kingsbury` dataset distributed with Matminer [34], which associates formation energies with specific crystal structures, allowing us to match our computed data with high confidence. Additional details about the dataset are provided in Appendix H.

For the majority of materials studied, the MAE in formation energy predicted by metaGGA functionals was ≈80-120 meV/atom. Strikingly, r^{2}SCAN formation energies had approximately 20% and 15% lower MAEs than SCAN for strongly- and weakly-bound materials, respectively, even though r^{2}SCAN is less theoretically exact (i.e., r^{2}SCAN relaxes the fourth order gradient expansion constraint for exchange that is satisfied by SCAN [25]). Although surprising from a theoretical standpoint, other recent studies have also reported greater accuracy of r^{2}SCAN compared to SCAN. For example, r^{2}SCAN was found to predict cohesive energies and bulk moduli of solids more accurately than SCAN [35].

We observed in Section III A that despite many materials having similar formation energies, there were a number of outlying materials for which $|\Delta H_f^{\mathrm{r^2SCAN}} - \Delta H_f^{\mathrm{SCAN}}| \geq$ 100-200 meV/atom or more. To evaluate the implications of such large differences, we examined the accuracy vs. experiment of all strongly- or weakly-bound materials for which $|\Delta H_f^{\mathrm{r^2SCAN}} - \Delta H_f^{\mathrm{SCAN}}| \geq 50$ meV/atom. There are 665 such materials in the entire dataset, of which we have experimental data for 345. Among this group of outliers, $\Delta H_f^{\mathrm{r^2SCAN}}$ is more accurate than $\Delta H_f^{\mathrm{SCAN}}$. Specifically, the mean error for r^{2}SCAN was −43.8 meV/atom, while the mean error for SCAN was −55.8 meV/atom, and the MAEs were 90.2 and 134.9 meV/atom for r^{2}SCAN and SCAN, respectively.

Comparing the metaGGA functionals to PBEsol, we note that for strongly-bound materials, both r^{2}SCAN and SCAN predicted formation energy much more accurately than PBEsol. This finding is similar to the previous observation by by Isaacs and Wolverton [12] that SCAN outperforms PBE for strongly-bound materials. For weakly-bound materials, however, SCAN was slightly less accurate than PBEsol (also consistent with previous findings [12]), whereas r^{2}SCAN was more accurate. Hence, r^{2}SCAN predicted formation energy more accurately than SCAN or PBEsol for all material categories. This is a fortuitous result: it appears that the regularization procedure used to create r^{2}SCAN not only enhances numerical stability but also improves accuracy in one of the few areas in which SCAN was less accurate than PBE. This may be coincidental, or it may suggest that the greater smoothness of the r^{2}SCAN potential energy surface (achieved by sacrficing the GE4X constraint) is beneficial to accuracy as well as computational reliability [31].

2. Lattice Volume

Figure 3b summarizes the performance of the three functionals for predicting cell volume using experimental data obtained from the Inorganic Crystal Structure Database (ICSD) [36]. For strongly-bound materials,

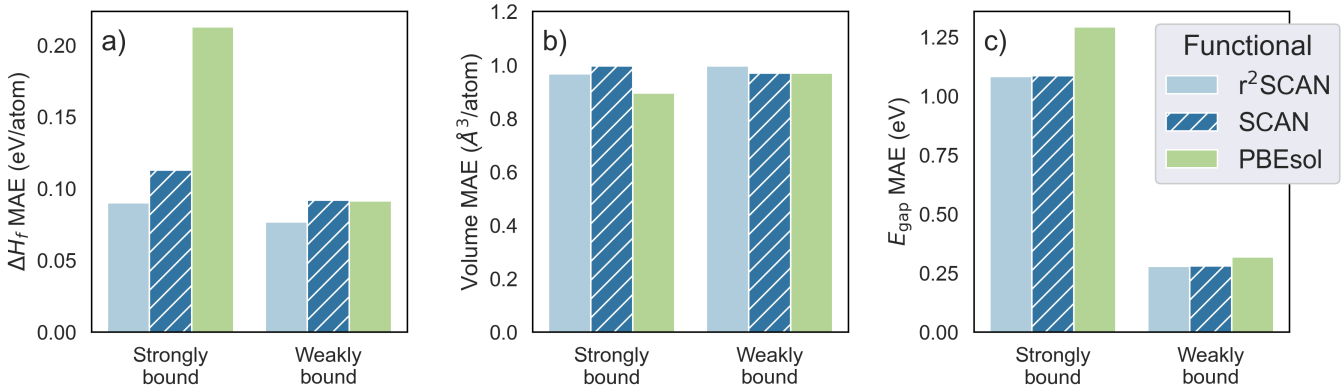

FIG. 3. Mean absolute error compared to experiment in a) formation energy (n=986 materials) b) cell volume (n=4,974 materials), and c) bandgap (n=582 materials) computed with r^{2}SCAN, SCAN, or PBEsol.

.

PBEsol has the lowest MAE of 0.89 Å^3/atom, followed by r^{2}SCAN (0.97 Å^3/atom) and SCAN (1.0 Å^3/atom). For weakly-bound materials, PBEsol and SCAN predict volume with a similar MAE of 0.97 Å^3/atom, while r^{2}SCAN has a slightly higher MAE of 1.0 Å^3/atom. Overall, neither metaGGA functional shows a clear and significant improvement in lattice volume prediction compared to PBEsol. Although surprising considering that SCAN lattice constants were shown to be more accurate than PBE (albeit underpredicted, whereas PBE lattice constants were overpredicted) [12], it is important to remember that PBEsol was developed specifically to reproduce solid lattice constants with high accuracy.

3. Bandgap

The errors in predicted bandgap are shown in Figure 3c for 582 materials that were present in both our dataset and the experimental `expt_gap_kingsbury` dataset in Matminer [34]. Compilation of the bandgap data is described in more detail in Appendix H.

For strongly-bound materials, the MAE in predicted bandgap was nearly identical between r^{2}SCAN and SCAN at 1.078 and 1.081 eV, respectively. The same was true for weakly-bound materials; although in this case the MAE was much lower at ≈0.28 eV. Although the MAEs for both metaGGA functionals were considerable, they were ≈0.21 eV and 0.04 eV lower than the PBEsol MAE for strongly- and weakly-bound materials, respectively.

C. Computational performance and reliability

Finally, we used the large amount of computed data we generated to develop a qualitative understanding of the relative computational demands and reliability of r^{2}SCAN and SCAN. In Figure 4a we present the relative performance of r^{2}SCAN, SCAN, and PBEsol in terms of 1) total CPU time, 2) total number of ionic steps and 3) total number of self consistent field (SCF) cycles (summed over all ionic steps) required to reach convergence. We note that this was not a rigorous computational benchmark, because the starting structures for the GGA and metaGGA stages of the workflow were not identical. As described in Section II A, each starting structure was optimized using equivalent VASP settings using both 1) PBE followed by SCAN and 2) PBEsol followed by r^{2}SCAN. All calculations were carried out on the Cori supercomputer at the National Energy Research Scientific Computing Center (Berkeley, CA); however the parallelization settings (i.e., number of nodes, cores, and multiprocessing tasks) varied slightly among calculations. As such, the information in Figure 4 should not be considered a definitive representation of the relative computational demands of these functionals, but rather a qualitative representation of their performance over a large and diverse set of materials.

As shown in the figure, r^{2}SCAN required approximately 0.5-2x the CPU time to converge as SCAN, and 0.5-1x the number of ionic and electronic steps. Compared to PBEsol, r^{2}SCAN required 2-4x the CPU time, 1-3x the number of ionic steps, and 1-2x the number of total SCF cycles. Our results here are largely consistent with a previous rigorous benchmark for CPU time based on single-point calculations, which showed that r^{2}SCAN required approximately 0.9x of the CPU time as SCAN and approximately 4x as much as PBE. [37] Our finding that fewer ionic steps are required is consistent with a study by Ning and co-workers [38] which found r^{2}SCAN to generate smoother potential energy surfaces (facilitating convergence) compared to SCAN. Thus, modestly fewer ionic steps and modestly less CPU time are required to converge r^{2}SCAN than SCAN, but both functionals require considerably more computational resources than PBEsol.

Time required for convergence does not tell the whole

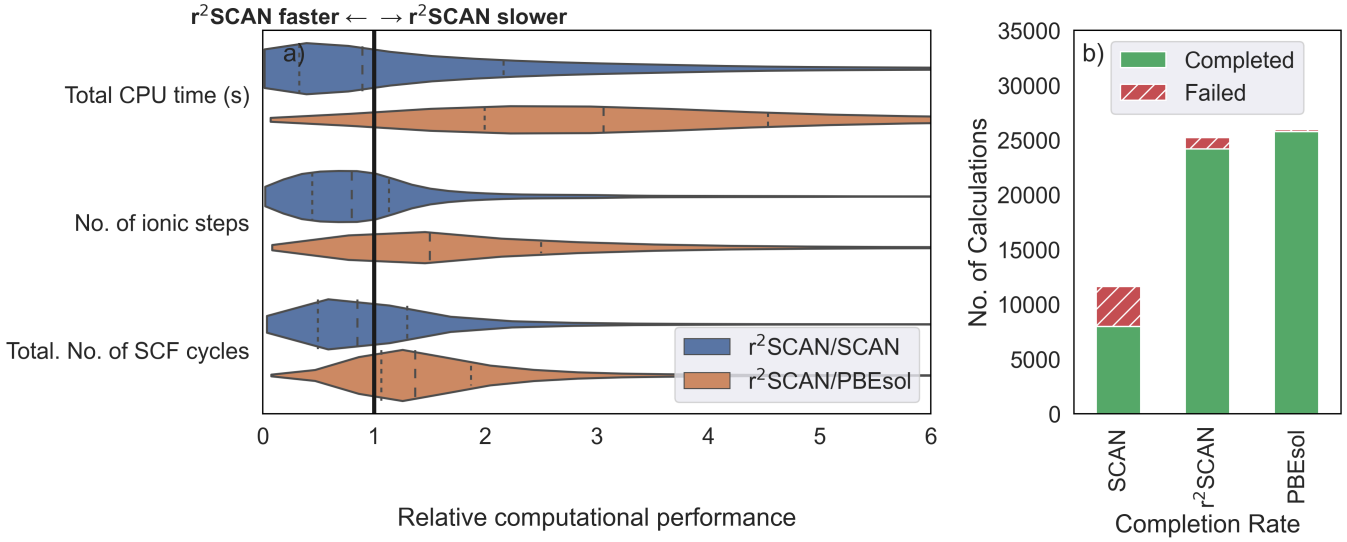

FIG. 4. a) Relative computational performance of r^{2}SCAN compared to SCAN (blue) or PBEsol (orange), demonstrating that computational time required for r^{2}SCAN is smaller than SCAN but larger than PBEsol. Each variable is plotted as the ratio of the value in the r^{2}SCAN calculation divided by the value in the corresponding SCAN or PBEsol calculation. Dashed lines inside each violin represent the quartiles of the distribution. b) Completion rate of calculations carried out using each density functional.

story, however, because the data in Figure 4a reflect only *successful* calculations, and hence mask the much more reliable convergence of r^{2}SCAN. Among approximately 11,000 and 25,000 total calculations we attempted with SCAN and r^{2}SCAN, respectively, we observed a completion rate of 96% for r^{2}SCAN, but only 69% for SCAN (Figure 4b). Calculations that did not complete either failed with unrecoverable errors or ran out of wall time. Again, although these failure statistics do not represent a rigorous comparison of the two functionals, they qualitatively highlight the generally much more reliable convergence of r^{2}SCAN compared to SCAN, which was a key objective of its development [25].

IV. SUMMARY AND OUTLOOK

In summary, we have compared r^{2}SCAN and SCAN predictions for key properties of approximately 6,000 solid materials. We find that r^{2}SCAN predicts substantially similar formation energies, bandgaps, and degrees of electron localization as the original SCAN functional, but predicts systematically larger lattice constants. r^{2}SCAN is found to predict formation energies more accurately than SCAN and PBEsol for both strongly- and weakly-bound materials, while r^{2}SCAN and SCAN calculated bandgaps are virtually identical and modestly more accurate than those predicted by PBEsol. For materials containing U, Np or Pu, r^{2}SCAN predicts formation energies that are substantially different from and considerably more accurate than those predicted by SCAN. The reason for this is not clear, and could arise from a fortuitous cancellation of errors related to the lack of spin-orbit-coupling in our calculations and/or as a consequence of the smoother potential energy surface generated by r^{2}SCAN. With respect to computational reliability, we find that r^{2}SCAN requires modestly fewer computational resources than SCAN, but offers much more reliable convergence. Thus, our large-scale benchmark confirms that r^{2}SCAN has delivered on its promises of numerical efficiency and accuracy [25], making it an ideal choice for high-throughput metaGGA calculations.

V. DATA AVAILABILITY

All data referenced herein are publicly available on Figshare [39] and will be integrated into the Materials Project database [30] in the near future. Our computational workflow has been implemented into the pymatgen [40], custodian [40], and atomate [41] packages as of versions 2020.12.3, 2021.1.8, and 0.9.6, respectively, for readers wishing to utilize it in their own work.

VI. ACKNOWLEDGEMENTS

We gratefully acknowledge James Furness and Jianwei Sun of Tulane University and Aaron Kaplan and John Perdew of Temple University for helpful discussions and assistance in compiling VASP with the r^{2}SCAN source code. This work was intellectually led by the Materials Project, which is funded by the U.S. Department of Energy, Office of Science, Office of Basic Energy Sciences,

Materials Sciences and Engineering Division, under Contract no. DE-AC02-05-CH11231: Materials Project program KC23MP. Additional support was also provided by the Data Infrastructure Building Blocks (DIBBS) Local Spectroscopy Data Infrastructure (LSDI) project funded by the National Science Foundation (NSF) under Award Number 1640899.

VII. AUTHOR CONTRIBUTIONS

Ryan Kingsbury: Conceptualization, Software, Methodology, Data Curation, Formal Analysis, Writing - Original Draft, Writing - Review & Editing. Christopher Bartel: Conceptualization, Writing - Review & Editing. Ayush Gupta: Formal Analysis, Writing - Review & Editing. Jason Munro: Methodology, Writing - Review & Editing. Matthew Horton: Conceptualization, Methodology, Writing - Review & Editing, Shyam Dwaraknath: Conceptualization, Methodology, Writing - Review & Editing, Supervision. Kristin Persson: Conceptualization, Writing - Review & Editing, Supervision, Funding Acquisition.

VIII. COMPETING INTEREST STATEMENT

The authors declare no competing financial interests.

IX. REFERENCES

[1] N. Mardirossian and M. Head-Gordon, Molecular Physics **115**, 2315 (2017).

[2] A. Jain, S. P. Ong, G. Hautier, W. Chen, W. D. Richards, S. Dacek, S. Cholia, D. Gunter, D. Skinner, G. Ceder, and K. A. Persson, APL Materials **1**, 011002 (2013).

[3] C. Draxl and M. Scheffler, MRS Bulletin **43**, 676–682 (2018).

[4] J. E. Saal, S. Kirklin, M. Aykol, B. Meredig, and C. Wolverton, JOM **65**, 1501 (2013).

[5] S. Kirklin, J. E. Saal, B. Meredig, A. Thompson, J. W. Doak, M. Aykol, S. Rühl, and C. Wolverton, npj Computational Materials **1**, 10.1038/npjcompumats.2015.10 (2015).

[6] L. Himanen, A. Geurts, A. S. Foster, and P. Rinke, Advanced Science **6**, 1900808 (2019).

[7] J. P. Perdew, K. Burke, and M. Ernzerhof, Phys. Rev. Lett. **77**, 3865 (1996).

[8] D. C. Langreth and J. P. Perdew, Physical Review B 10.1103/PhysRevB.21.5469 (1980).

[9] J. P. Perdew, A. Ruzsinszky, G. I. Csonka, O. A. Vydrov, G. E. Scuseria, L. A. Constantin, X. Zhou, and K. Burke, Phys. Rev. Lett. **100**, 136406 (2008).

[10] J. P. Perdew, MRS Bulletin **38**, 743 (2013).

[11] S. Grimme, A. Hansen, J. G. Brandenburg, and C. Bannwarth, Chemical Reviews **116**, 5105 (2016).

[12] E. B. Isaacs and C. Wolverton, Physical Review Materials **2**, 1 (2018).

[13] J. H. Yang, D. A. Kitchaev, and G. Ceder, Physical Review B **100**, 035132 (2019).

[14] S. Lany and A. Zunger, Phys. Rev. B **78**, 235104 (2008).

[15] Y. Si, M. Li, Z. Zhou, M. Liu, and O. Prezhdo, The Journal of chemical physics **152**, 024706 (2020), publisher: AIP Publishing, LLC.

[16] J. Sun, A. Ruzsinszky, and J. Perdew, Physical Review Letters **115**, 1 (2015).

[17] Y. Zhang, D. A. Kitchaev, J. Yang, T. Chen, S. T. Dacek, R. A. Sarmiento-Pérez, M. A. Marques, H. Peng, G. Ceder, J. P. Perdew, and J. Sun, npj Computational Materials **4**, 10.1038/s41524-018-0065-z (2018).

[18] W. Sun, A. Holder, B. Orvañanos, E. Arca, A. Zakutayev, S. Lany, and G. Ceder, Chemistry of Materials **29**, 6936 (2017).

[19] J.-S. Park, Current Applied Physics **22**, 61 (2021).

[20] C. J. Bartel, A. W. Weimer, S. Lany, C. B. Musgrave, and A. M. Holder, npj Computational Materials **5**, 10.1038/s41524-018-0143-2 (2019).

[21] Y. Fu and D. J. Singh, Physical Review B **100**, 045126 (2019).

[22] F. Tran, G. Baudesson, J. Carrete, G. K. H. Madsen, P. Blaha, K. Schwarz, and D. J. Singh, Shortcomings of meta-gga functionals when describing magnetism (2020), arXiv:2004.04543 [cond-mat.mtrl-sci].

[23] J. S. Rego and M. de Konig, Journal of Chemical Physics **152**, 10.1063/1.5142710 (2020).

[24] D. Mejia-Rodriguez and S. B. Trickey, Physical Review B **98**, 10.1103/physrevb.98.115161 (2018).

[25] J. W. Furness, A. D. Kaplan, J. Ning, J. P. Perdew, and J. Sun, The Journal of Physical Chemistry Letters **11**, 8208 (2020).

[26] G. Kresse and J. Furthmüller, Computational Materials Science **6**, 15 (1996).

[27] G. Kresse and J. Furthmüller, Phys. Rev. B **54**, 11169 (1996).

[28] P. E. Blöchl, Phys. Rev. B **50**, 17953 (1994).

[29] P. Wisesa, K. A. McGill, and T. Mueller, Physical Review B **93**, 1 (2016).

[30] S. P. Ong, S. Cholia, A. Jain, M. Brafman, D. Gunter, G. Ceder, and K. A. Persson, Computational Materials Science **97**, 209 (2015).

[31] A. D. Kaplan, J. W. Furness, L. Hou, J. Sun, and J. P. Perdew, personal communication (2021).

[32] O. Y. Long, G. Sai Gautam, and E. A. Carter, Phys. Rev. Materials **4**, 045401 (2020).

[33] P. Fuentealba, E. Chamorro, and J. C. Santos, in *Theoretical and Computational Chemistry*, Vol. 19 (Elsevier B.V., 2007) pp. 57–85, iSSN: 13807323.

[34] L. Ward, A. Dunn, A. Faghaninia, N. E. Zimmermann, S. Bajaj, Q. Wang, J. Montoya, J. Chen, K. Bystrom, M. Dylla, K. Chard, M. Asta, K. A. Persson, G. J. Snyder, I. Foster, and A. Jain, Computational Materials Science **152**, 60 (2018).

[35] D. Mejía-Rodríguez and S. B. Trickey, Physical Review B **102**, 121109 (2020).

[36] I. Levin, Nist inorganic crystal structure database (icsd) (2020).

[37] D. Mejía-Rodríguez and S. B. Trickey, The Journal of Physical Chemistry A **124**, 9889 (2020).

[38] J. Ning, J. W. Furness, and J. Sun, Reliable lattice dynamics from an efficient density functional (2021), arXiv:2107.11850 [cond-mat.mtrl-sci].

[39] R. Kingsbury, C. J. Bartel, S. Dwaraknath, A. Gupta, J. M. Munro, M. Horton, and K. Persson, r2scan, scan, and pbesol calcluations for 6,307 solid materials (2021).

[40] S. P. Ong, W. D. Richards, A. Jain, G. Hautier, M. Kocher, S. Cholia, D. Gunter, V. L. Chevrier, K. A. Persson, and G. Ceder, Computational Materials Science **68**, 314 (2013).

[41] K. Mathew, J. H. Montoya, A. Faghaninia, S. Dwarakanath, M. Aykol, H. Tang, I. Chu, T. Smidt, B. Bocklund, M. Horton, J. Dagdelen, B. Wood, Z.-K. Liu, J. Neaton, S. P. Ong, K. Persson, and A. Jain, Computational Materials Science **139**, 140 (2017).

[42] S. Curtarolo, W. Setyawan, S. Wang, J. Xue, K. Yang, R. H. Taylor, L. J. Nelson, G. L. Hart, S. Sanvito, M. Buongiorno-Nardelli, N. Mingo, and O. Levy, Computational Materials Science **58**, 227 (2012).

[43] K. Choudhary and F. Tavazza, Computational Materials Science **161**, 300 (2019).

[44] A. M. Ganose, A. J. Jackson, and D. O. Scanlon, Journal of Open Source Software **3**, 717 (2018).

[45] S. Lany, Physical Review B - Condensed Matter and Materials Physics **78**, 1 (2008).

[46] B. Silvi and A. Savin, Nature **371**, 683 (1994).

[47] M. Yu and D. R. Trinkle, The Journal of Chemical Physics **134**, 064111 (2011).

[48] W. Tang, E. Sanville, and G. Henkelman, Journal of Physics: Condensed Matter **21**, 084204 (2009).

[49] J. W. Furness, personal communication (2021).

[50] L. Ward, A. Dunn, A. Faghaninia, N. E. Zimmermann, S. Bajaj, Q. Wang, J. Montoya, J. Chen, K. Bystrom, M. Dylla, K. Chard, M. Asta, K. A. Persson, G. J. Snyder, I. Foster, and A. Jain, Computational Materials Science **152**, 60 (2018).

[51] O. Kubaschewski, C. Alcock, and P. Spencer, *Materials Thermochemistry*, 6th ed. (Pergamon Press, 1993).

[52] M. W. Chase, Nist-janaf thermochemical tables (1998).

[53] G. Kim, S. V. Meschel, P. Nash, and W. Chen, Scientific Data **4**, 10.1038/sdata.2017.162 (2017).

[54] G. Kim, S. Meschel, P. Nash, and W. Chen, Experimental formation enthalpies for intermetallic phases and other inorganic compounds (2017).

[55] A. Wang, R. Kingsbury, M. McDermott, M. Horton, A. Jain, S. P. Ong, S. Dwaraknath, and K. Persson, A framework for quantifying uncertainty in dft energy corrections (2021).

[56] Y. Zhuo, A. M. Tehrani, and J. Brgoch, The Journal of Physical Chemistry Letters **9**, 1668 (2018).

X. APPENDICES

Appendix A: Workflow development

a. Design

Historically, it has been common practice in the Materials Project [2] and AFLOW [42] to perform two structure optimization calculations in series for any given material. The purpose of this double optimization is to make the calculations more robust to changes in the size or shape of the unit cell during the calculation. If the cell changes size, for example, then the initial wavefunctions and k-point grid are not rigorously valid. Performing a double optimization allows them to be re-initialized to account for the changed unit cell.

Taking inspiration from this model, we tested five workflow designs incorporating 1) an initial GGA calculation followed by 2) one or two metaGGA optimizations. The initial GGA precondition step serves two purposes in addition to helping account for changes in the unit cell. First, it accelerates convergence of the subsequent metaGGA calculations by generating an initial guess of the optimized structure and charge density. Second, it provides an estimate of the material's bandgap that we use to select an appropriate value of KSPACING for the subsequent metaGGA step (see next section).

Comparative testing of different workflow designs was carried out using PBE [7] and SCAN [16] for the GGA and metaGGA steps, respectively. The five workflow designs compared several different strategies, including 1) whether to use a single point or full structure optimization during the GGA preconditiong step, 2) whether to use force convergence criteria for all steps or only the final step and 3) whether to enable van der Waals corrections in the metaGGA steps (see Table A.1). Among the five designs, we observed that there were significant (≈5%) changes in cell volume between the GGA precondition step and the first metaGGA relaxation, but negligible (<0.5%) changes in cell volume during the second metaGGA relaxation. We also observed fewer failed calculations when all calculations were force-converged. Hence, for the final workflow design we eliminated the 2nd metaGGA structure optimization and employed a force-converged criteria for both GGA and metaGGA optimizations.

TABLE A.1. Workflow designs[a]

	1	2	3	4	5
GGA precondition	PBE static	PBE opt. (F)	PBE opt. (F)	PBE opt. (E)	PBE opt. (F)
metaGGA optimization 1	SCAN (F)	SCAN (F)	SCAN (E)	SCAN (E)	SCAN+rvv10 (F)
metaGGA optimization 2	SCAN (F)	SCAN (F)	SCAN (E)	SCAN (E)	SCAN+rvv10 (F)
No. of failed calculations	2 / 30	2 / 30	4/30	6/ 30	2 / 30
Avg. change in cell volume from optimization 1 to 2	0.34%	−0.03%	−0.09%	−0.06%	0.35%

[a] E = energy converged, F = force and energy converged, rvv10 = Van der Waals correction

b. Plane-wave energy cutoff and k-point density convergence

We next determined an appropriate plane-wave energy cutoff and k-point density for our workflow through a series of formation energy convergence tests. We selected 21 materials representing a diversity of chemical systems and computed the formation energy of each by subtracting the energies of the corresponding elemental references. The structures selected for benchmarking were obtained from the from the Materials Project [30] database and are listed in Table A.2.

We performed single point (static) energy calculations on each material using plane-wave energy cutoff (ENCUT) values of 520, 680, 850, 1000, and 1200 eV. Rather than specifying the number of k-points explicitly, we specified a KSPACING in the VASP INCAR file, which is the approach currently recommended by the VASP developers [26, 27]. Since non-metallic systems generally require fewer k-points for good convergence than metallic systems [43], we used the GGA-estimated bandgap of each material to select a KSPACING value ranging from 0.22 Å^{-1} (metals) to 0.44 Å^{-1} (insulators). Between these two limits, KSPACING is calculated as a continuous function of the bandgap according to: [29]

$$r_{\min} = 25.22 - 2.87 E_{\text{gap}} \tag{A1}$$

$$\text{KSPACING} = 1.0265 \left(\frac{2\pi}{r_{\min} - 1.0183} \right) \tag{A2}$$

where $r_{\min}$ is the minimum distance between k-points on the real-space superlattice and E_{gap} is the bandgap in eV. Thus, a lower KSPACING value corresponds to a larger $r_{\min}$ and a denser k-point grid [29]. Conversions between $r_{\min}$ and KSPACING are provided in Table A.3 and Figure A.1.

Our selection of KSPACING values was informed by the work of Wisesa et al. [29], who found that KSPACING= 0.54 and 0.22 Å^{-1} for metallic and non-metallic systems, respectively, resulted in approximately 80% of calculations converging within 1 meV/atom. As a point of comparison, the Materials Project historically used a k-point density of 1000 k-points per reciprocal atom, which would yield similar convergence to an $r_{\min}$ of 24.7 Å [29], which corresponds to a KSPACING of 0.254 Å^{-1}. As an additional point of reference for convergence testing, we also performed static calculations with a tighter KSPACING of 0.1 Å^{-1} at ENCUT values of 680 eV and 1200 eV.

In a prelminary phase of workflow development (not reported here), we performed this convergence testing using PBE followed by SCAN. For the final results reported here, we used the PBEsol [9] GGA functional to perform the first optimization because it is generally more accurate than PBE for solid lattice parameters, and we used r^{2}SCAN [25] for the metaGGA step. By comparing the data from both benchmarking exercises, we confirmed that the ENCUT and KSPACING settings we selected for the PBEsol/r^{2}SCAN workflow are also appropriate for PBE/SCAN.

Convergence results are shown for each material in Figures A.2 - A.22. The formation energies determined with an ENCUT value of 680 eV converged within 1 meV/atom of the 1200 eV result for 17 out of 20 materials (in 1 case, the 1200 eV energy could not be determined due to computational difficulties). Among the remaining 3 materials, one (LiN) was converged within 1.5 meV/atom. For the two other materials (MoS_2 and CeO_2), ENCUT values were converged within 1 meV/atom of the 1000 eV cutoff, but the formation energy increased abruptly between 1000 eV and 1200 eV by 20 meV/atom. The origin of this abrupt change in energy is not clear. However, since the formation energy was well-converged over the range of other ENCUT values, which are more feasible for high throughput workflows, we did not investigate it further.

KSPACING convergence was possible to evaluate only for 10 materials, because computational limitations prevented the 0.1 Å^{-1} / 1200 eV calculation from completing for the remaining materials. The default KSPACING setting was converged within 1 meV/atom for 6 out of 10 and within 3 meV/atom for 9 out of 10 materials. The one remaining material (CeO_2) did not converge because of the abrupt change in energy at ENCUT=1200 eV noted above. For this material, the default KSPACING and KSPACING=0.1 scenarios were within 1 meV/atom of one another.

Based on these convergence tests, we concluded that a plane wave energy cutoff of 680 eV and a bandgap-determined KSPACING value between 0.22 and 0.44 Å^{-1} should lead to well-converged formation energies (within 1-2 meV/atom) for the majority of materials.

TABLE A.2. Materials used to benchmark energy convergence.

Formula	Spacegroup Symbol	Materials Project ID [30]
AlN	$P6_3mc$	mp-661
Al_2O_3	$R\bar{3}c$	mp-1143
BN	$P6_3/mmc$	mp-984
$BaBeSiO_4$	Cm	mp-550751
CeO_2	$Fm\bar{3}m$	mp-20194
CaF_2	$Fm\bar{3}m$	mp-2741
EuO	$Fm\bar{3}m$	mp-21394
FeP	Pnma	mp-1005
FeS	P4/nmm	mp-505531
GaAs	$F\bar{4}3m$	mp-2534
InSb	$F\bar{4}3m$	mp-20012
LiH	$Fm\bar{3}m$	mp-23703
LiF	$Fm\bar{3}m$	mp-1138
LiCl	$P6_3mc$	mp-1185319
Li_2O	$Fm\bar{3}m$	mp-1960
LiN	$I\bar{4}m2$	mp-1059612
MoS_2	$P\bar{3}m1$	mp-1027525
NaI	$Fm\bar{3}m$	mp-23268
SrI_2	Pnma	mp-568284
TiO_2	C2/m	mp-554278
VO_2	$P2_1/c$	mp-1102963

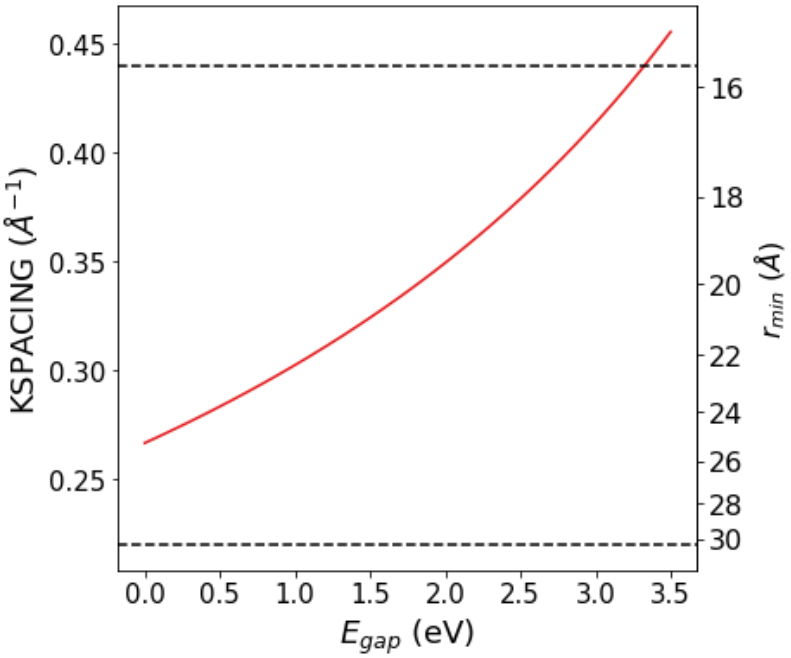

FIG. A.1. Conversion of KSPACING to $r_{\min}$ values. KSPACING values are constrained to the range 0.22-0.44, as indicated by the dashed horizontal lines.

TABLE A.3. Conversion of KSPACING to r_{min} (Å) values.

KSPACING (Å^{-1})	r_{min} (Å)
0.17	39
0.22	30
0.28	24
0.34	20
0.44	16
0.54	13
0.63	11
0.73	10

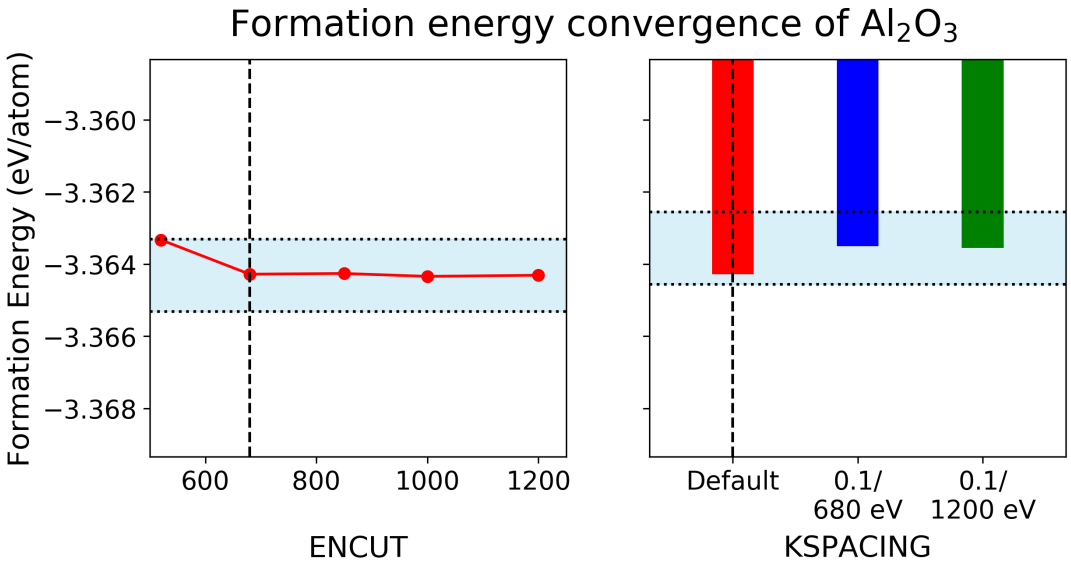

FIG. A.2. Formation energy convergence of static r^{2}SCAN calculations. Shading indicates convergence within 1 meV of the calculation with ENCUT = 1200 eV. In some cases, the calculations with ENCUT=1200 eV or KSPACING = 0.1 failed to converge, in which case shading and the corresponding bars or points are not shown. The dashed vertical line indicates the final setting chosen for the computational workflow (ENCUT=680 eV, 0.22 $\leq$ KSPACING $\leq$ 0.44).

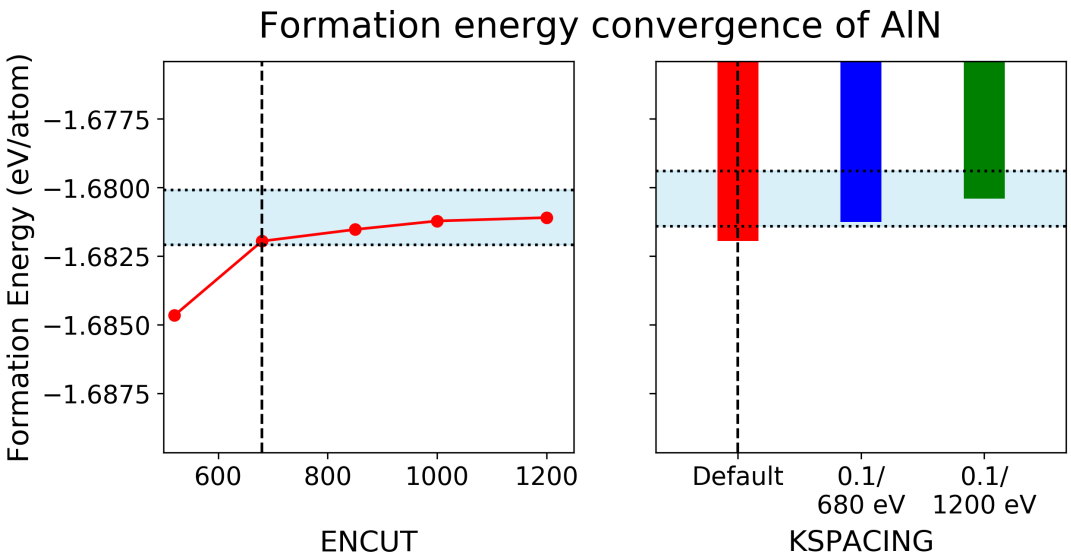

FIG. A.3. Formation energy convergence of static r^{2}SCAN calculations. Shading indicates convergence within 1 meV of the calculation with ENCUT = 1200 eV. In some cases, the calculations with ENCUT=1200 eV or KSPACING = 0.1 failed to converge, in which case shading and the corresponding bars or points are not shown. The dashed vertical line indicates the final setting chosen for the computational workflow (ENCUT=680 eV, 0.22 ≤ KSPACING ≤ 0.44).

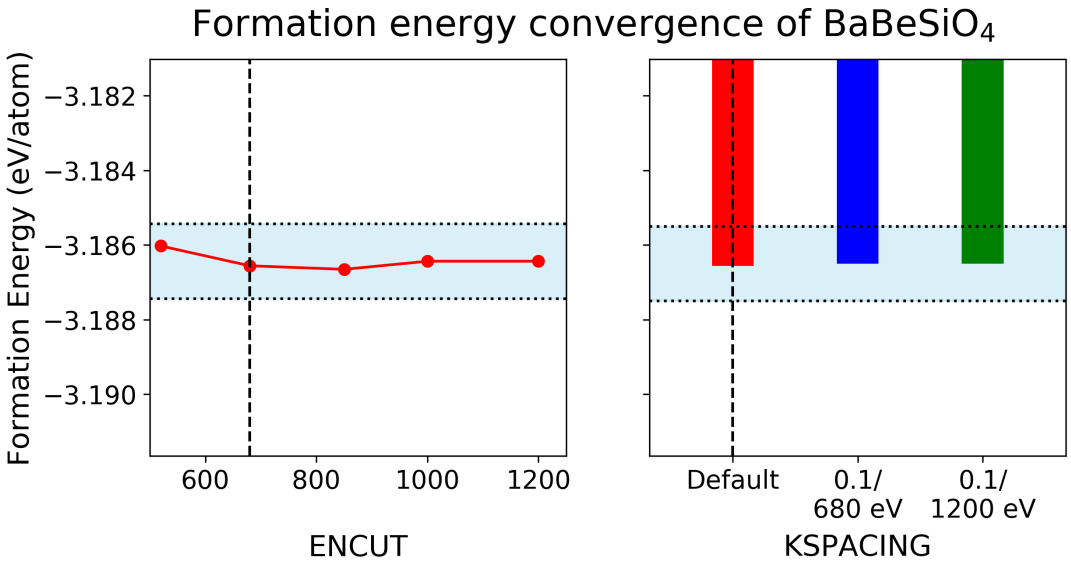

FIG. A.4. Formation energy convergence of static r^{2}SCAN calculations. Shading indicates convergence within 1 meV of the calculation with ENCUT = 1200 eV. In some cases, the calculations with ENCUT=1200 eV or KSPACING = 0.1 failed to converge, in which case shading and the corresponding bars or points are not shown. The dashed vertical line indicates the final setting chosen for the computational workflow (ENCUT=680 eV, 0.22 ≤ KSPACING ≤ 0.44).

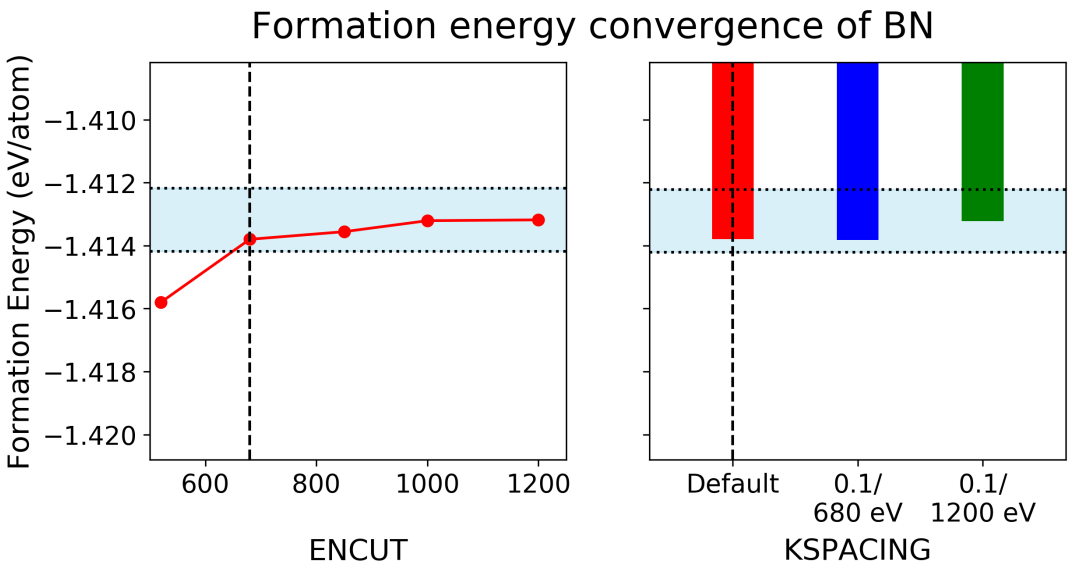

FIG. A.5. Formation energy convergence of static r^{2}SCAN calculations. Shading indicates convergence within 1 meV of the calculation with ENCUT = 1200 eV. In some cases, the calculations with ENCUT=1200 eV or KSPACING = 0.1 failed to converge, in which case shading and the corresponding bars or points are not shown. The dashed vertical line indicates the final setting chosen for the computational workflow (ENCUT=680 eV, 0.22 $\leq$ KSPACING $\leq$ 0.44).

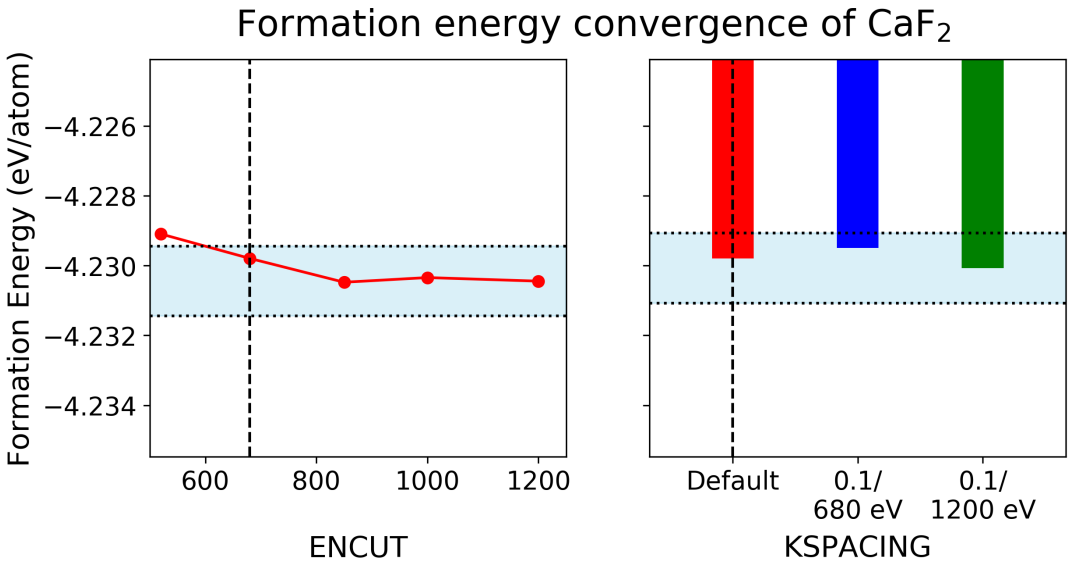

FIG. A.6. Formation energy convergence of static r^{2}SCAN calculations. Shading indicates convergence within 1 meV of the calculation with ENCUT = 1200 eV. In some cases, the calculations with ENCUT=1200 eV or KSPACING = 0.1 failed to converge, in which case shading and the corresponding bars or points are not shown. The dashed vertical line indicates the final setting chosen for the computational workflow (ENCUT=680 eV, 0.22 $\leq$ KSPACING $\leq$ 0.44).

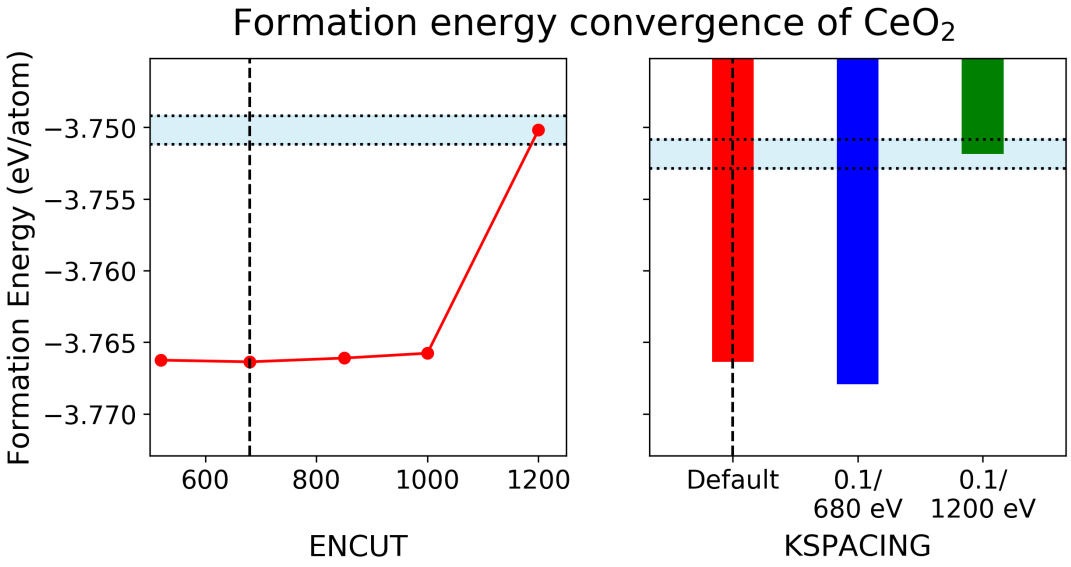

FIG. A.7. Formation energy convergence of static r^{2}SCAN calculations. Shading indicates convergence within 1 meV of the calculation with ENCUT = 1200 eV. In some cases, the calculations with ENCUT=1200 eV or KSPACING = 0.1 failed to converge, in which case shading and the corresponding bars or points are not shown. The dashed vertical line indicates the final setting chosen for the computational workflow (ENCUT=680 eV, 0.22 $\leq$ KSPACING $\leq$ 0.44).

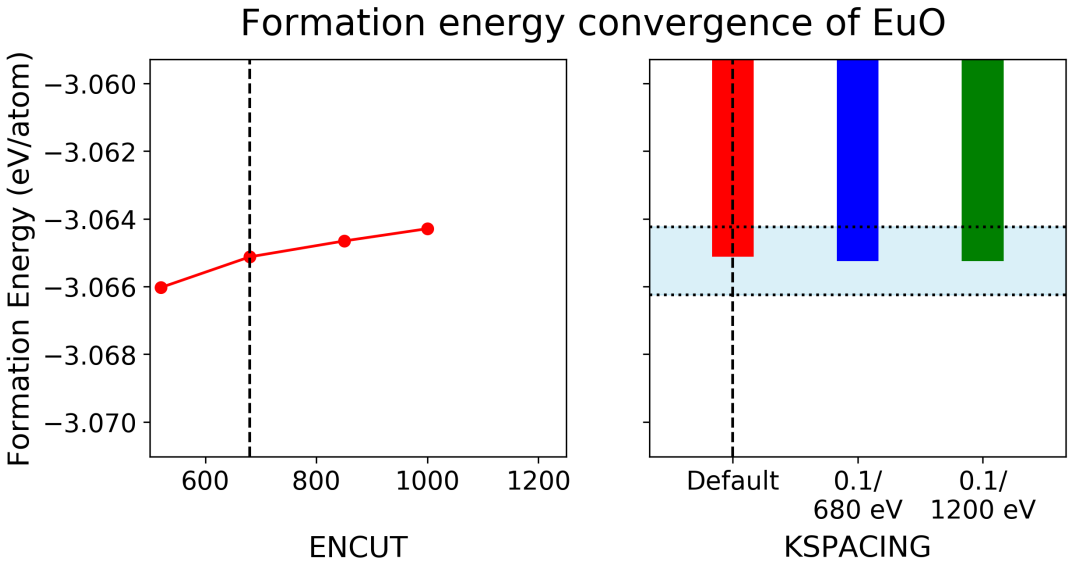

FIG. A.8. Formation energy convergence of static r^{2}SCAN calculations. Shading indicates convergence within 1 meV of the calculation with ENCUT = 1200 eV. In some cases, the calculations with ENCUT=1200 eV or KSPACING = 0.1 failed to converge, in which case shading and the corresponding bars or points are not shown. The dashed vertical line indicates the final setting chosen for the computational workflow (ENCUT=680 eV, 0.22 $\leq$ KSPACING $\leq$ 0.44).

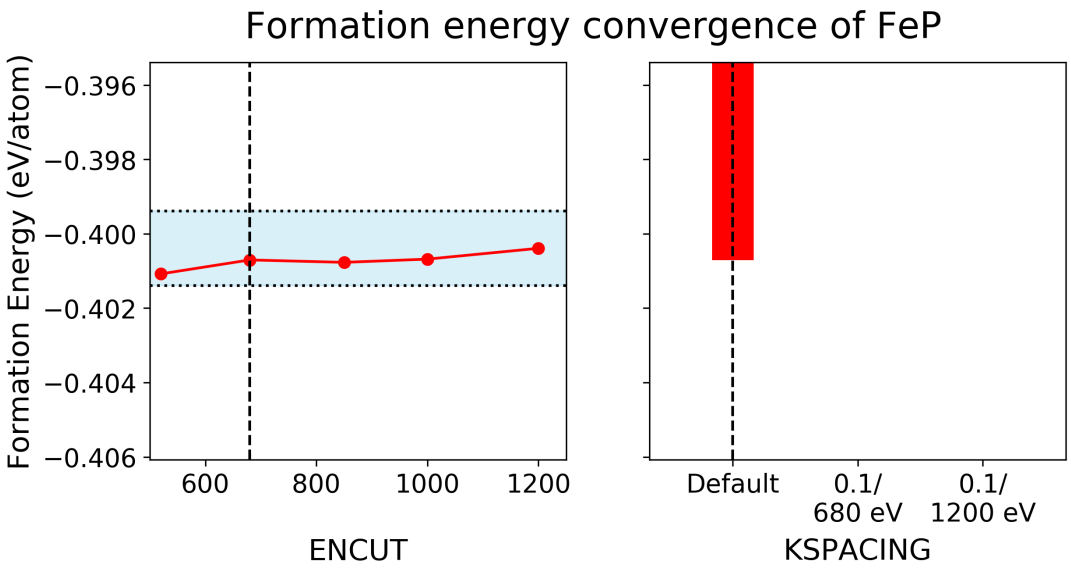

FIG. A.9. Formation energy convergence of static r^{2}SCAN calculations. Shading indicates convergence within 1 meV of the calculation with ENCUT = 1200 eV. In some cases, the calculations with ENCUT=1200 eV or KSPACING = 0.1 failed to converge, in which case shading and the corresponding bars or points are not shown. The dashed vertical line indicates the final setting chosen for the computational workflow (ENCUT=680 eV, 0.22 $\leq$ KSPACING $\leq$ 0.44).

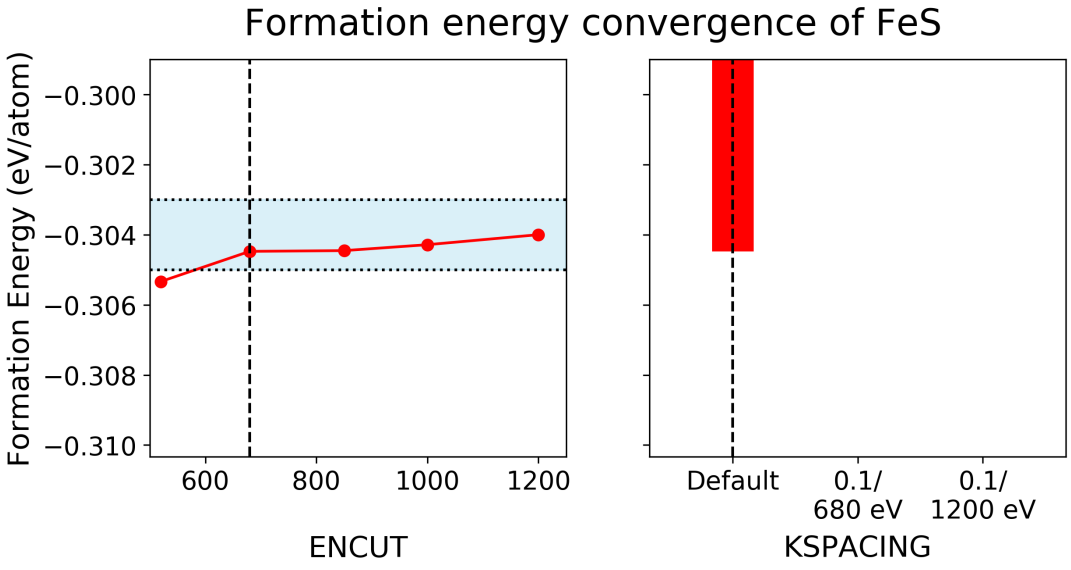

FIG. A.10. Formation energy convergence of static r^{2}SCAN calculations. Shading indicates convergence within 1 meV of the calculation with ENCUT = 1200 eV. In some cases, the calculations with ENCUT=1200 eV or KSPACING = 0.1 failed to converge, in which case shading and the corresponding bars or points are not shown. The dashed vertical line indicates the final setting chosen for the computational workflow (ENCUT=680 eV, 0.22 $\leq$ KSPACING $\leq$ 0.44).

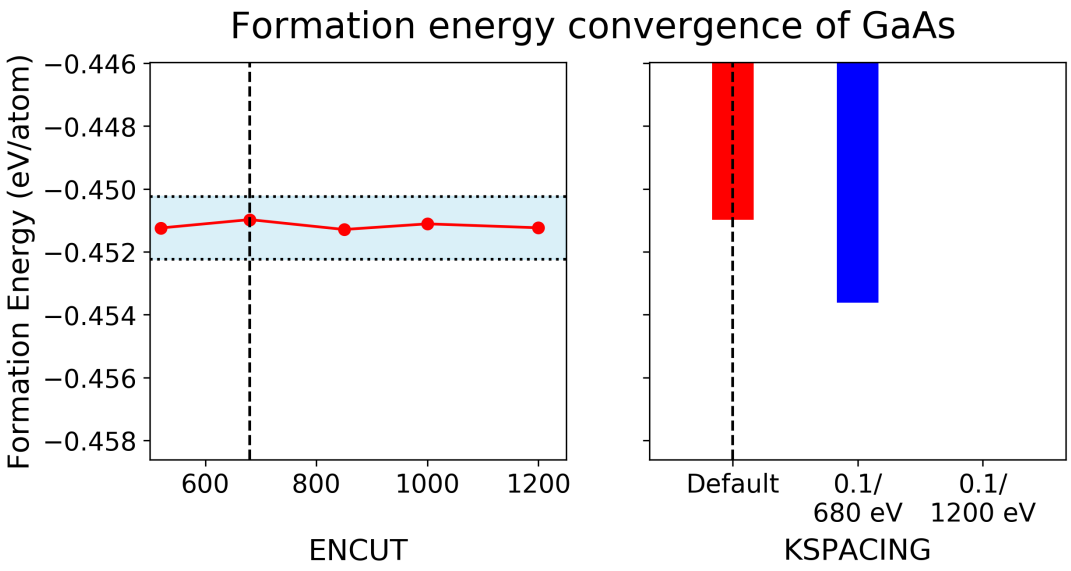

FIG. A.11. Formation energy convergence of static r^{2}SCAN calculations. Shading indicates convergence within 1 meV of the calculation with ENCUT = 1200 eV. In some cases, the calculations with ENCUT=1200 eV or KSPACING = 0.1 failed to converge, in which case shading and the corresponding bars or points are not shown. The dashed vertical line indicates the final setting chosen for the computational workflow (ENCUT=680 eV, 0.22 $\leq$ KSPACING $\leq$ 0.44).

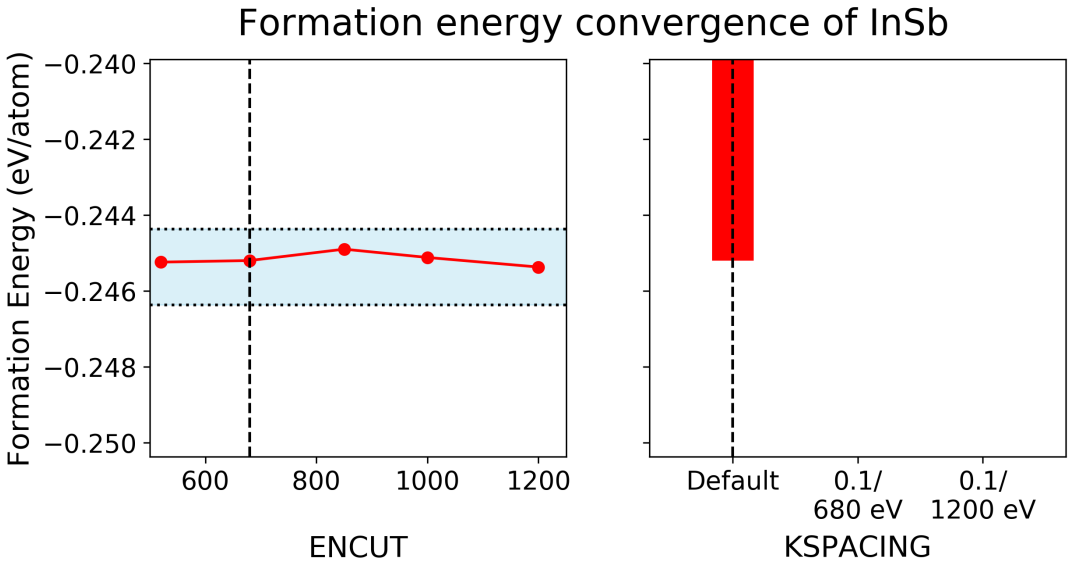

FIG. A.12. Formation energy convergence of static r^{2}SCAN calculations. Shading indicates convergence within 1 meV of the calculation with ENCUT = 1200 eV. In some cases, the calculations with ENCUT=1200 eV or KSPACING = 0.1 failed to converge, in which case shading and the corresponding bars or points are not shown. The dashed vertical line indicates the final setting chosen for the computational workflow (ENCUT=680 eV, 0.22 $\leq$ KSPACING $\leq$ 0.44).

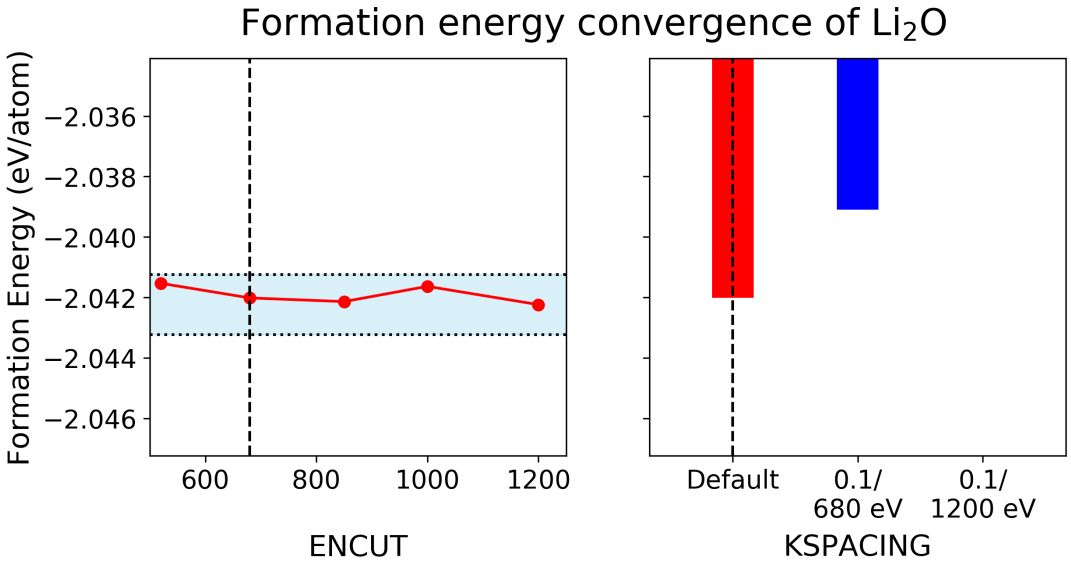

FIG. A.13. Formation energy convergence of static r^{2}SCAN calculations. Shading indicates convergence within 1 meV of the calculation with ENCUT = 1200 eV. In some cases, the calculations with ENCUT=1200 eV or KSPACING = 0.1 failed to converge, in which case shading and the corresponding bars or points are not shown. The dashed vertical line indicates the final setting chosen for the computational workflow (ENCUT=680 eV, 0.22 $\leq$ KSPACING $\leq$ 0.44).

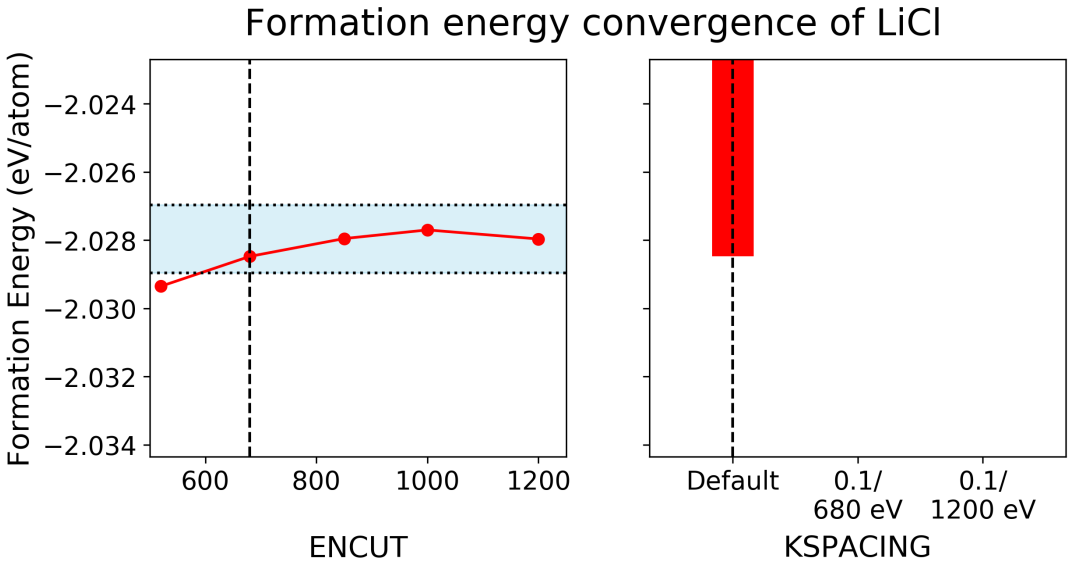

FIG. A.14. Formation energy convergence of static r^{2}SCAN calculations. Shading indicates convergence within 1 meV of the calculation with ENCUT = 1200 eV. In some cases, the calculations with ENCUT=1200 eV or KSPACING = 0.1 failed to converge, in which case shading and the corresponding bars or points are not shown. The dashed vertical line indicates the final setting chosen for the computational workflow (ENCUT=680 eV, 0.22 $\leq$ KSPACING $\leq$ 0.44).

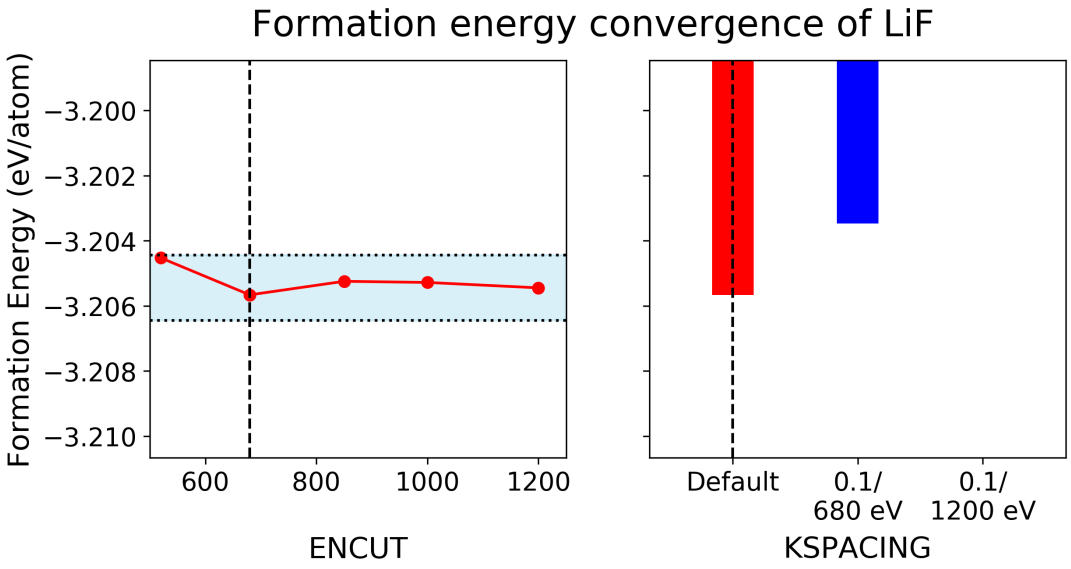

FIG. A.15. Formation energy convergence of static r^{2}SCAN calculations. Shading indicates convergence within 1 meV of the calculation with ENCUT = 1200 eV. In some cases, the calculations with ENCUT=1200 eV or KSPACING = 0.1 failed to converge, in which case shading and the corresponding bars or points are not shown. The dashed vertical line indicates the final setting chosen for the computational workflow (ENCUT=680 eV, 0.22 $\leq$ KSPACING $\leq$ 0.44).

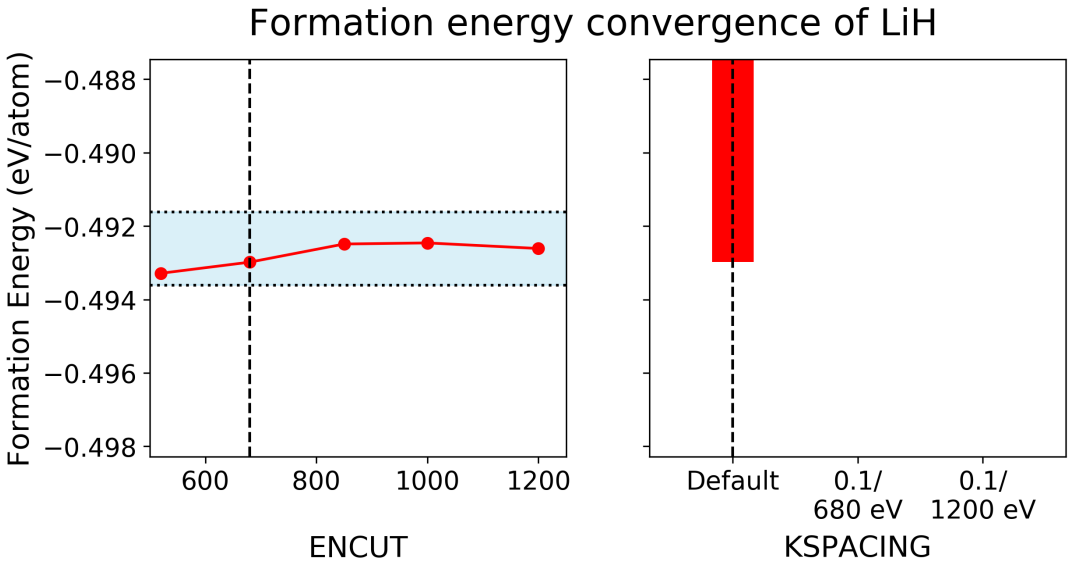

FIG. A.16. Formation energy convergence of static r^{2}SCAN calculations. Shading indicates convergence within 1 meV of the calculation with ENCUT = 1200 eV. In some cases, the calculations with ENCUT=1200 eV or KSPACING = 0.1 failed to converge, in which case shading and the corresponding bars or points are not shown. The dashed vertical line indicates the final setting chosen for the computational workflow (ENCUT=680 eV, 0.22 $\leq$ KSPACING $\leq$ 0.44).

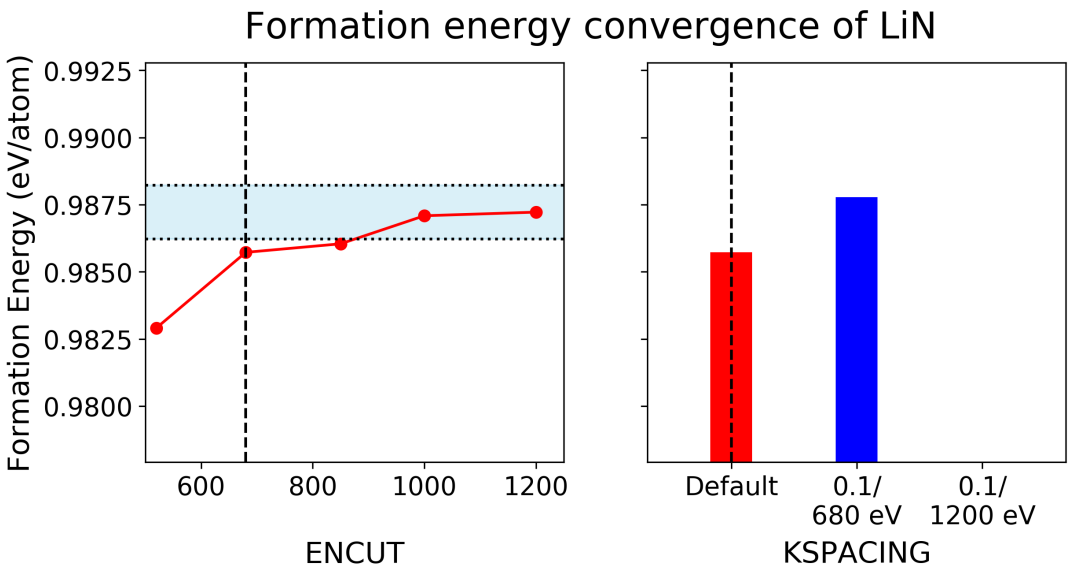

FIG. A.17. Formation energy convergence of static r^{2}SCAN calculations. Shading indicates convergence within 1 meV of the calculation with ENCUT = 1200 eV. In some cases, the calculations with ENCUT=1200 eV or KSPACING = 0.1 failed to converge, in which case shading and the corresponding bars or points are not shown. The dashed vertical line indicates the final setting chosen for the computational workflow (ENCUT=680 eV, 0.22 $\leq$ KSPACING $\leq$ 0.44).

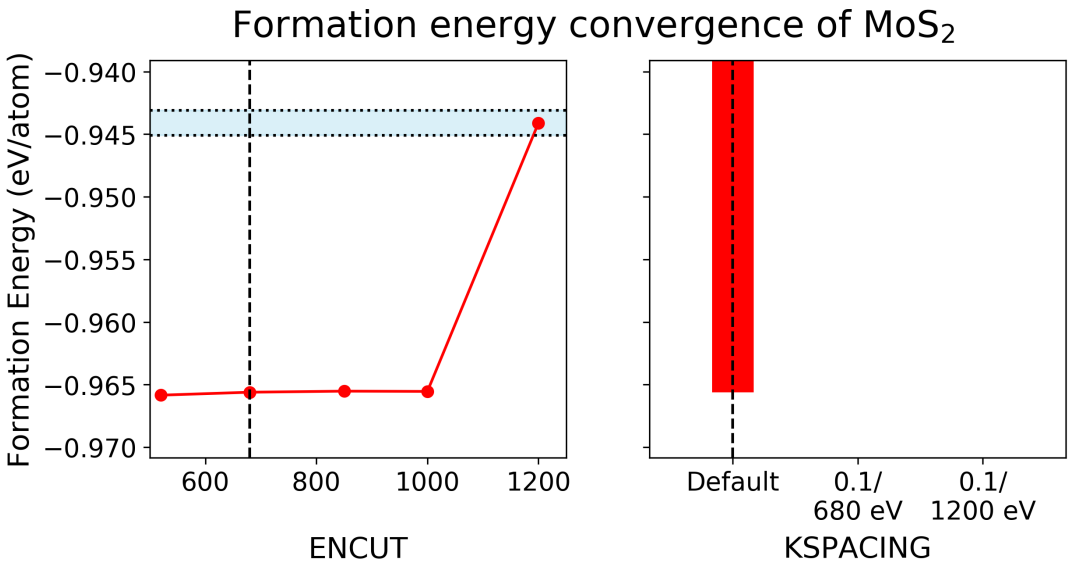

FIG. A.18. Formation energy convergence of static r^{2}SCAN calculations. Shading indicates convergence within 1 meV of the calculation with ENCUT = 1200 eV. In some cases, the calculations with ENCUT=1200 eV or KSPACING = 0.1 failed to converge, in which case shading and the corresponding bars or points are not shown. The dashed vertical line indicates the final setting chosen for the computational workflow (ENCUT=680 eV, 0.22 $\leq$ KSPACING $\leq$ 0.44).

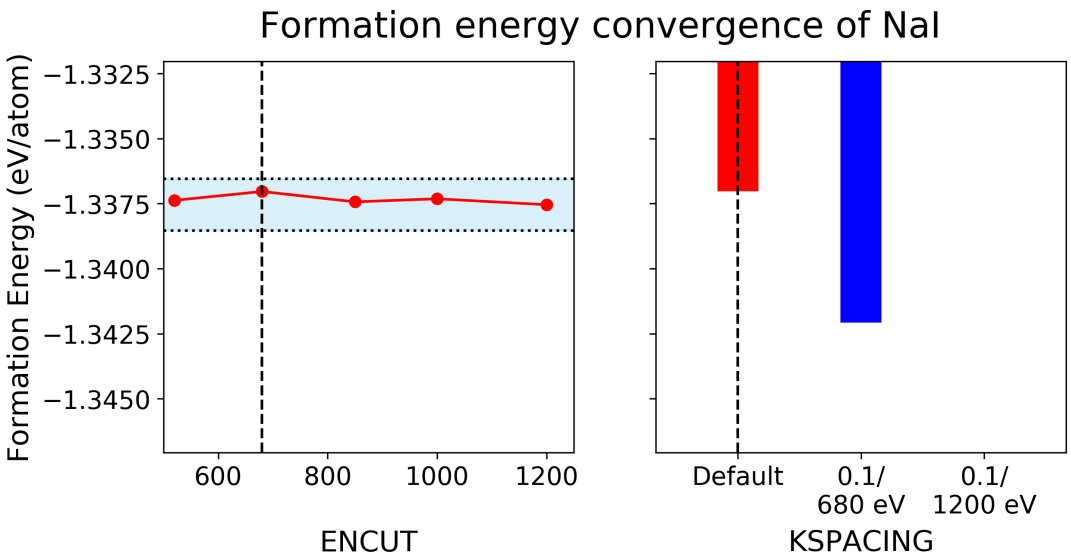

FIG. A.19. Formation energy convergence of static r^{2}SCAN calculations. Shading indicates convergence within 1 meV of the calculation with ENCUT = 1200 eV. In some cases, the calculations with ENCUT=1200 eV or KSPACING = 0.1 failed to converge, in which case shading and the corresponding bars or points are not shown. The dashed vertical line indicates the final setting chosen for the computational workflow (ENCUT=680 eV, 0.22 ≤ KSPACING ≤ 0.44).

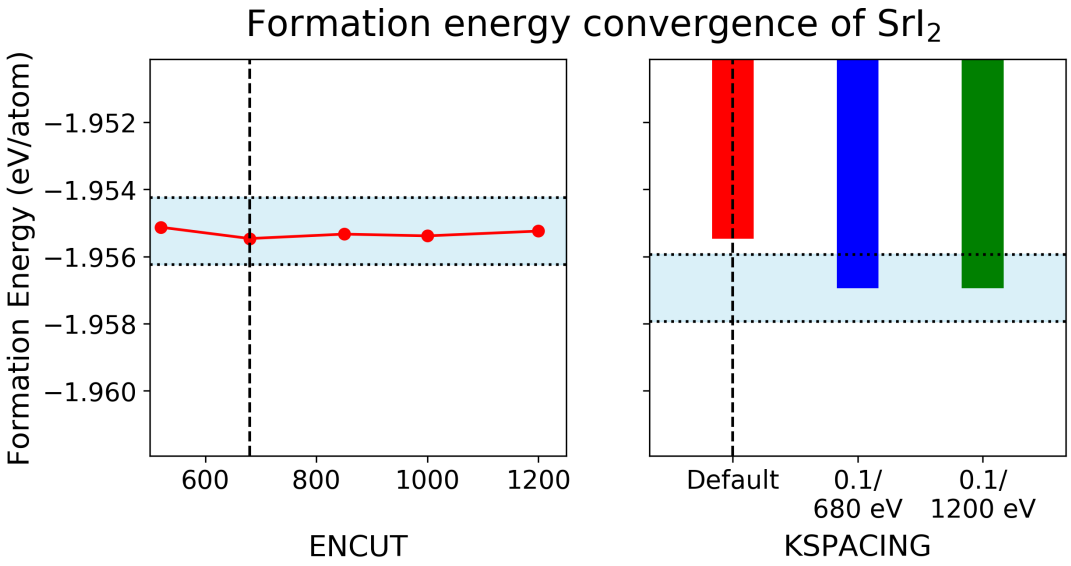

FIG. A.20. Formation energy convergence of static r^{2}SCAN calculations. Shading indicates convergence within 1 meV of the calculation with ENCUT = 1200 eV. In some cases, the calculations with ENCUT=1200 eV or KSPACING = 0.1 failed to converge, in which case shading and the corresponding bars or points are not shown. The dashed vertical line indicates the final setting chosen for the computational workflow (ENCUT=680 eV, 0.22 ≤ KSPACING ≤ 0.44).

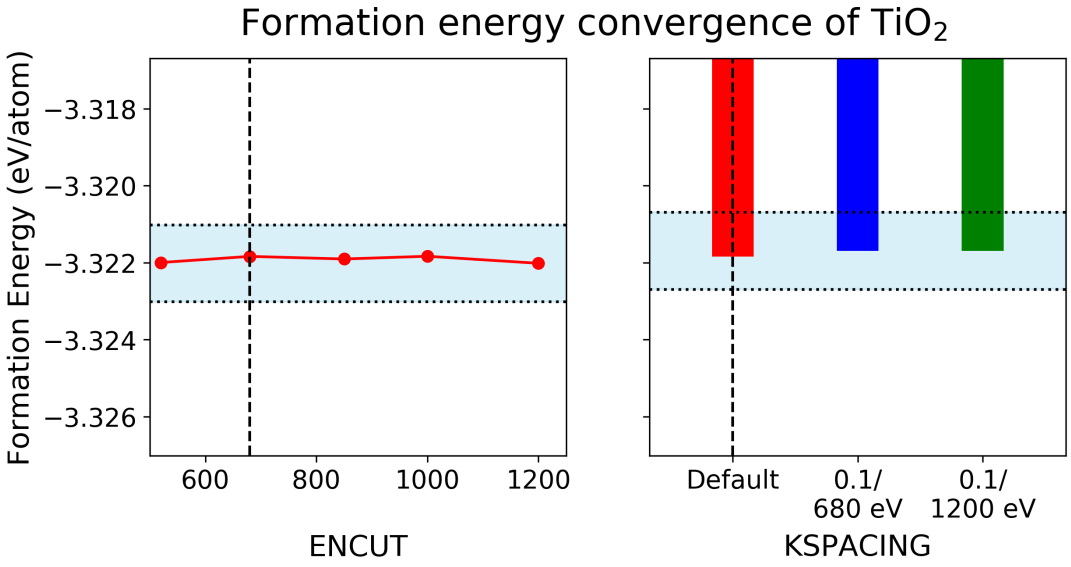

FIG. A.21. Formation energy convergence of static r^{2}SCAN calculations. Shading indicates convergence within 1 meV of the calculation with ENCUT = 1200 eV. In some cases, the calculations with ENCUT=1200 eV or KSPACING = 0.1 failed to converge, in which case shading and the corresponding bars or points are not shown. The dashed vertical line indicates the final setting chosen for the computational workflow (ENCUT=680 eV, 0.22 $\leq$ KSPACING $\leq$ 0.44).

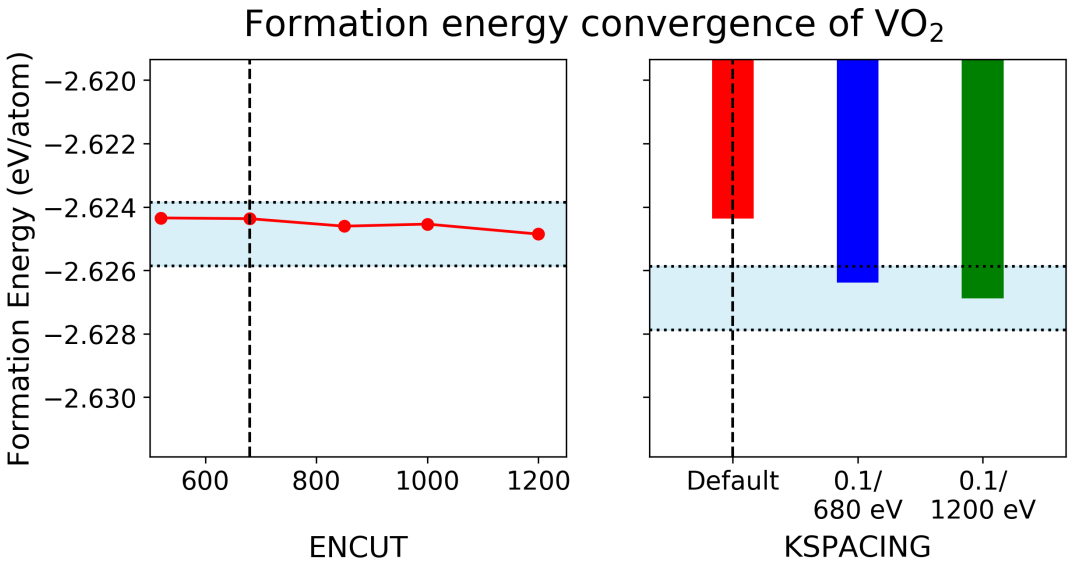

FIG. A.22. Formation energy convergence of static r^{2}SCAN calculations. Shading indicates convergence within 1 meV of the calculation with ENCUT = 1200 eV. In some cases, the calculations with ENCUT=1200 eV or KSPACING = 0.1 failed to converge, in which case shading and the corresponding bars or points are not shown. The dashed vertical line indicates the final setting chosen for the computational workflow (ENCUT=680 eV, 0.22 $\leq$ KSPACING $\leq$ 0.44).

Appendix B: Cases of qualitative disagreement in metallic character

TABLE B.1: Cases of qualitative disagreement between r^{2}SCAN and SCAN in the metallic or insulating character of a material. Cases in which predicted bandgaps disagree by $\gtrsim 1$ eV are highlighted in **bold font**.

Material ID	Formula	$E_{\text{gap}}^{\text{r}^2\text{SCAN}}$ (eV)	$E_{\text{gap}}^{\text{SCAN}}$ (eV)
mp-2832	Cr2Se3	0.0000	0.0032
mp-559435	CoF3	0.0000	0.0119
mp-1168	HfTe5	0.0000	0.0139
mp-999143	SrPd	0.0000	0.0148
mp-2142	Te2Os	0.0000	0.0251
mp-7302	CrP4	0.0000	0.0304
mp-1936	TaAs	0.0000	0.0327
mp-656887	Ni3O4	0.0000	0.0332
mp-20633	PbO2	0.0000	0.0775
mp-19871	PbAu2	0.0000	0.0811
mp-2733	Al8Mo3	0.0000	0.0942
mp-795	LiSi	0.0000	0.0988
mp-9429	USe3	0.0000	0.1175
mp-1192044	ZrCl3	0.0000	0.1262
mp-7898	Rb3As	0.0000	0.1328
mp-567510	BaSn2	0.0000	0.2130
mp-2480	OsSe2	0.0000	0.2397
mp-861727	PuBr2	0.0000	0.2769
mp-29950	Nb3Cl8	0.0000	0.3260
mp-11108	SrP3	0.0000	0.3673
mp-23223	TiI3	0.0000	0.4426
mp-19142	Mn2V2O7	0.0000	0.4484
mp-1225059	FeCl4	0.0000	0.5583
mp-14107	NpF3	0.0000	0.5698
mp-571143	TiCl3	0.0000	0.5980
mp-2804	LaP2	0.0000	0.7922
mp-1024969	**NpF5**	**0.0000**	**0.9807**
mp-2455	**As2Os**	**0.0000**	**0.9898**
mp-1186069	**Na(MoSe)3**	**0.0000**	**1.0002**
mp-1104255	**Sb2F13**	**0.0000**	**4.2005**
mp-542313	Ce2O3	0.0267	0.0000
mp-1018663	CeS2	0.0339	0.0000
mp-1007661	InSb	0.0353	0.0000
mp-8601	Te4Mo3	0.0540	0.0000
mp-1106024	Eu5As3	0.0576	0.0000
mp-861975	PaO3	0.0653	0.0000
mp-29621	Ba5Bi3	0.0678	0.0000
mp-569388	Te2Ir	0.0702	0.0000
mp-540671	Ti7Cl16	0.0761	0.0000
mp-30794	Na15Sn4	0.0805	0.0000
mp-1076951	CeNiGe	0.0814	0.0000
mp-20305	InAs	0.0851	0.0000
mp-22942	BaBiO3	0.1039	0.0000
mp-4083	MgCuAs	0.1065	0.0000
mp-9530	Y4C7	0.1145	0.0000
mp-1007652	InAs	0.1251	0.0000
mp-7570	RuF3	0.1272	0.0000
mp-19225	FeAgO2	0.1430	0.0000
mp-1101892	CeAs2	0.1433	0.0000
mp-569095	Rb3Bi	0.1630	0.0000
mp-23679	PuH3	0.1829	0.0000
mp-27258	P3Au2	0.1924	0.0000
mp-15700	Zn3As2	0.2167	0.0000
mp-20905	OsS2	0.2235	0.0000
mp-1025373	TcF6	0.2501	0.0000

mp-568753	TcBr3	0.2658	0.0000
mp-20724	Mg2Pb	0.2713	0.0000
mp-27838	Na3Bi	0.2787	0.0000
mp-569850	CeBr3	0.2824	0.0000
mp-22735	Ca2Sn	0.3358	0.0000
mp-1018059	GaSb	0.3735	0.0000
mp-1156	GaSb	0.3774	0.0000
mp-568002	HfI3	0.3838	0.0000
mp-32606	Ba3P2	0.3840	0.0000
mp-1317	CoSb3	0.4053	0.0000
mp-1201	Sb2Te3	0.4520	0.0000
mp-2008	FeAs2	0.5437	0.0000
mp-27974	PuBr3	0.6421	0.0000
mp-23247	ZrBr3	0.6614	0.0000
mp-27655	Te2I	0.6935	0.0000
mp-635413	Cs3Bi	0.7957	0.0000
mp-16608	**Si3Os2**	**0.9849**	**0.0000**
mp-567431	**ThCl4**	**4.2044**	**0.0000**

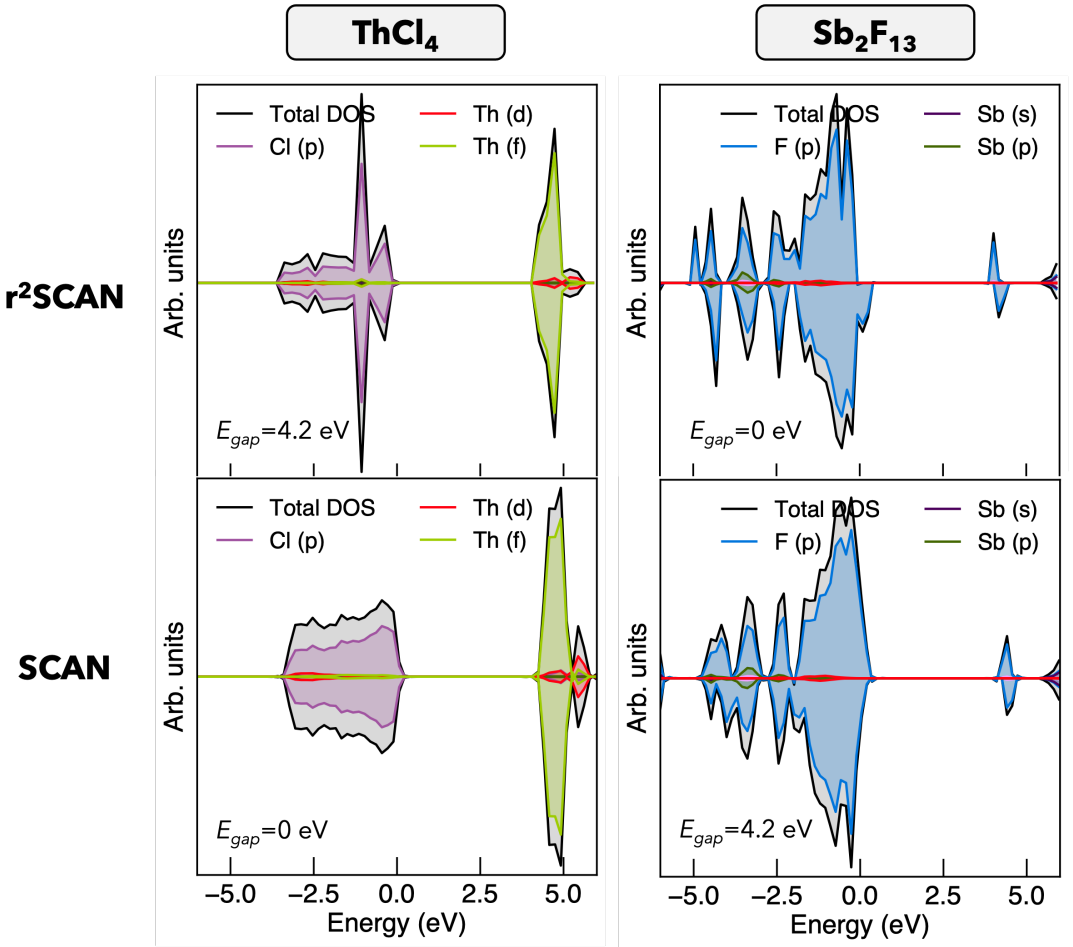

FIG. B.1. Example density of states (DOS) plots for materials where SCAN and r^{2}SCAN predict significantly different metallic or insulating character. The examples shown are the cases of largest positive and negative disagreement in the bandgap ($ThCl_4$ and Sb_2F_{13}, respectively). Insets indicate the bandgap as predicted by VASP. DOS plots were generated using `sumo` [44].

Appendix C: Elemental representation among studied materials

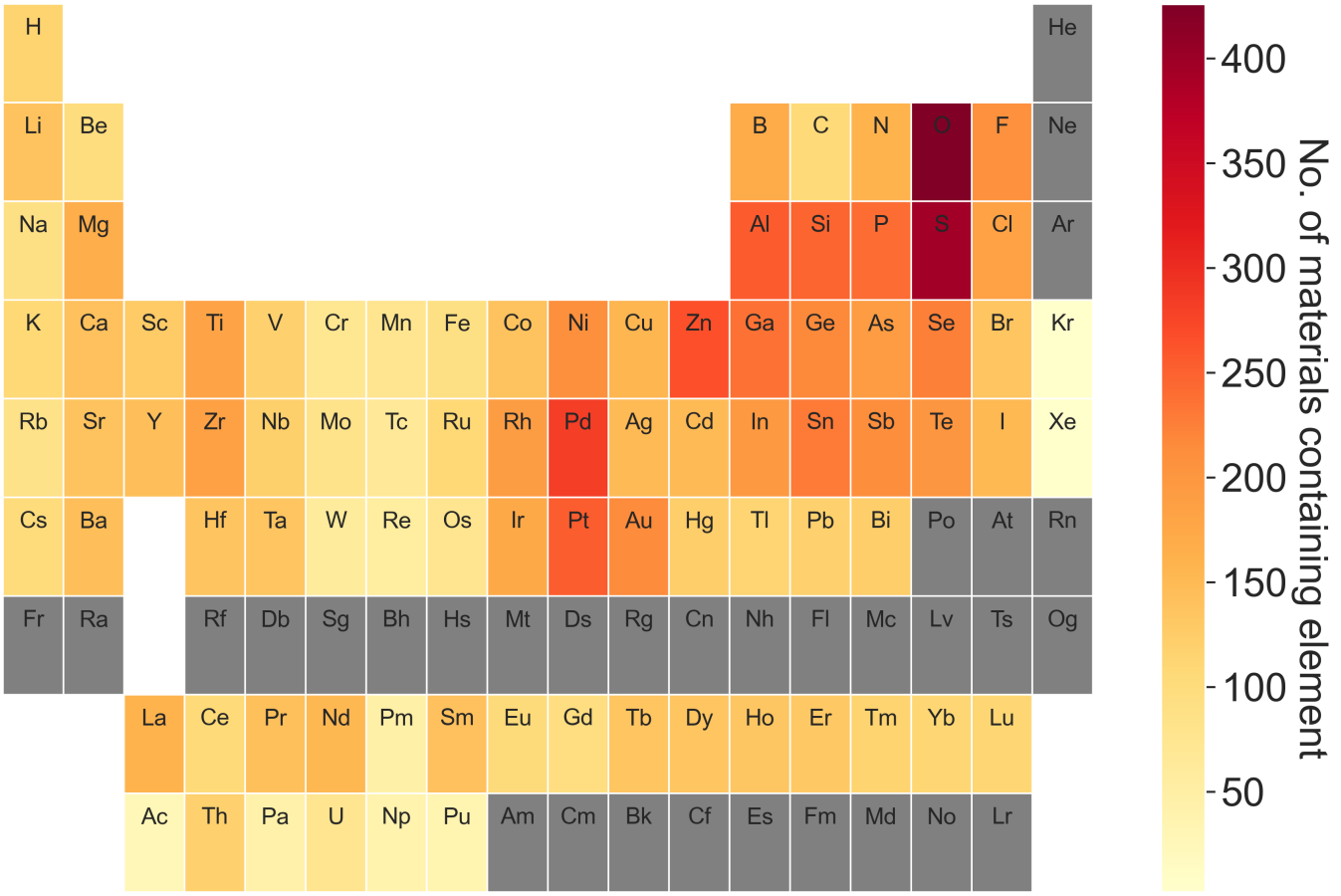

FIG. C.1. Representation of elements among the materials evaluated in this study. The periodic table is colored according to how many materials contained each element. Hence, TiO_2 would add one unit to both the Ti and O boxes.

Appendix D: Anomalous behavior of materials containing U, Np, or Pu

Materials containing U, Np, or Pu (n=150 materials) were found to exhibit exceptionally large differences in r^{2}SCAN formation energy compared to SCAN. Specifically, r^{2}SCAN formation energies for many U, Np or Pu-containing materials were much more negative (by up to 0.75 eV/atom) than those predicted by SCAN (Figure D.1a). The largest discrepancies appear to be associated specifically with compounds that also contain late transition metals or metalloids such as Sn, Sb, Te, As, or Se (Figure G.3). The materials with the largest discrepancies in formation energy do not exhibit systematic differences in other properties (e.g. volumes, bandgaps, or ΔELF_f, see Figure D.1b-d). Median volumes per atom predicted by r^{2}SCAN were 4.0% (0.7 Å^3/atom) larger than the SCAN predicted volumes on average (vs. 1.4-1.8% larger for strongly- and weakly-bound materials), while r^{2}SCAN bandgaps were within −0.16 to +0.28 eV of the SCAN predictions for 95% of materials in this category.

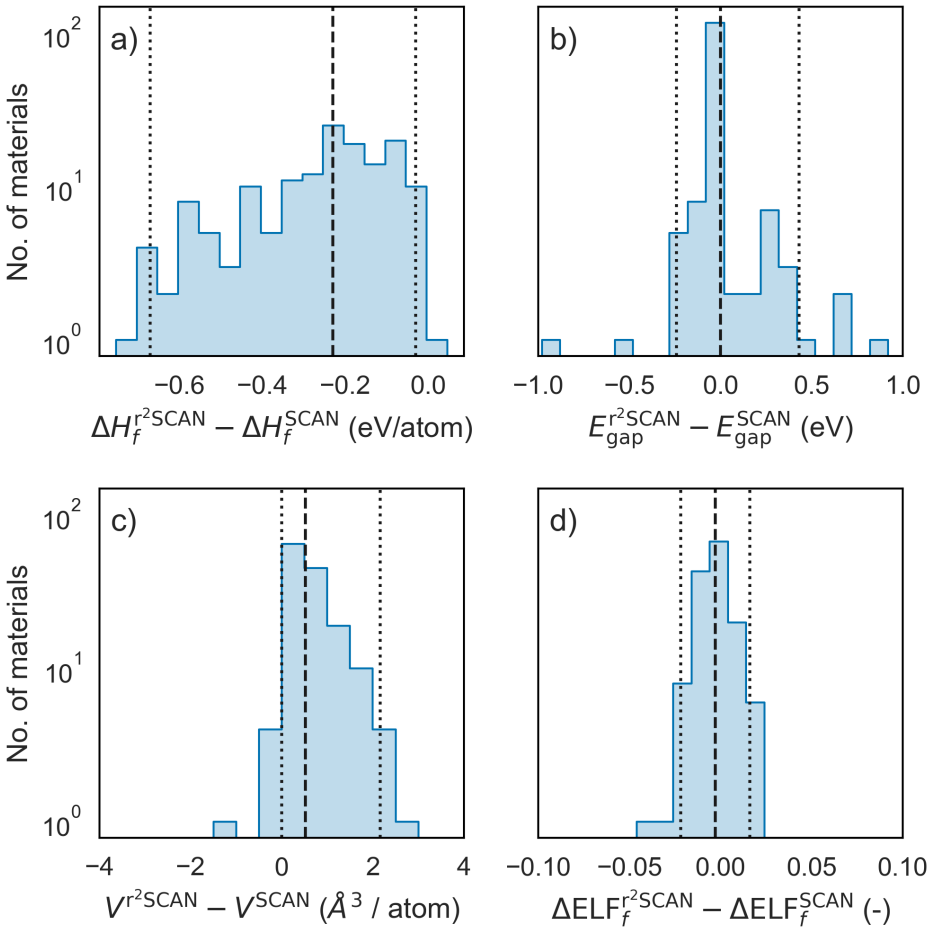

FIG. D.1. Changes in a) formation energy, b) bandgap, c) cell volume, and d) formation electron localization function (ΔELF_f; see Appendix E) when computed in r^{2}SCAN vs SCAN for materials containing U, Np, or Pu. Note that the y axis is logarithmic. Dashed and dotted vertical lines represent the median differences and two-sided 95th percentile differences, respectively,.

The anomalously high differences in formation energy for materials containing U, Np, or Pu may indicate that these chemistries are particularly sensitive to the differences in construction between r^{2}SCAN and SCAN (i.e., the omission of the fourth order gradient expansion constraint for exchange). It may also be a consequence of the fact that our calculations were run without spin-orbit coupling, which is typically required for accurate energies of heavy elements. We omitted spin-orbit coupling because our objective in this work was to develop a general-purpose workflow suited primarily to main group and transition metal compounds.

We also examined errors with respect to experimental formation energies and lattice volumes among materials containing U, Np, or Pu (Figure D.2). Strikingly, the MAE in formation energy predicted by r^{2}SCAN was 50% lower than that of SCAN. The poor accuracy of SCAN describing Np compounds is consistent with previous work: in their benchmark of the original SCAN functional, Isaacs and Wolverton [12] fit corrections to SCAN formation energies using

a FERE approach [45] and found that the chemical potential of Np had to be adjusted by ≈1 eV/atom to minimize error with respect to experiment. This was the largest adjustment fitted to any element studied. Considering that our calculations did not include spin-orbit coupling, it is unclear whether the superior accuracy of r^{2}SCAN formation energies compared to SCAN is simply a fortuitous coincidence, or an indication of inaccuracies in the SCAN description of U, Np, or Pu.

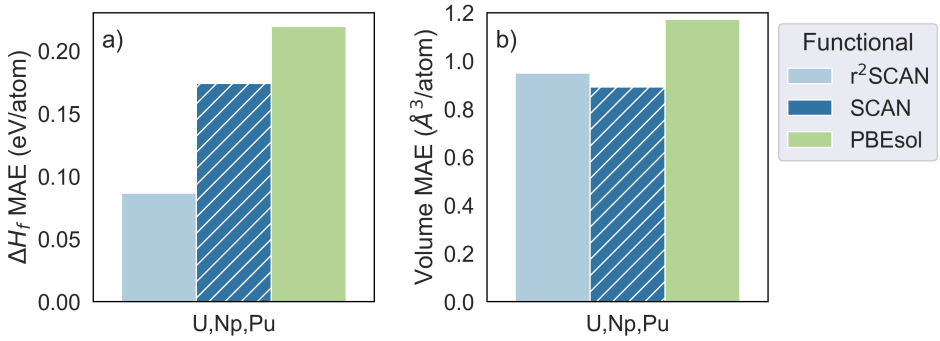

FIG. D.2. Mean absolute error compared to experiment in a) formation energy (n=30 materials) and b) cell volume (n=127 materials) computed with r^{2}SCAN, SCAN, or PBEsol.

.

With respect to lattice volumes, both metaGGA functionals achieved considerably lower MAEs than PBEsol (0.89 and 0.95 Å^3/atom for SCAN and r^{2}SCAN, respectively, vs. 1.17 Å^3/atom for PBEsol). Hence, the dramatic discrepancy we observed between r^{2}SCAN and SCAN formation energies is not evident in predictions of the lattice parameters.

Appendix E: Analysis of electron localization

Differences in the treatment of electron localization by r^{2}SCAN and SCAN were quantified via analysis of the electron localization function (ELF) [46]. We used Bader analysis [47, 48] to partition the charge density data generated by each VASP calculation into basins corresponding to each atom in a material's structure. We then used these basin assignments as a 'mask' on the ELF data to obtain statistics about the degree of electron localization around each atom in the material.

By analogy to the formation energy, we next calculated a "formation ELF" with respect to elemental references. We first determined the ELF values associated with each element in a material. For example, for the compound PtO_2, we averaged the ELF values in the regions associated with Pt (as determined by Bader analysis of the charge density), and then averaged ELF values in regions associated with O. We then subtracted the average ELF from calculations of the corresponding elemental references to obtain a "formation ELF", $\Delta\mathrm{ELF}_f$ as

$$\Delta\mathrm{ELF}_f = \sqrt{\sum_i^N \frac{(\mathrm{ELF_{i,cpd}} - \mathrm{ELF_{i,el}})^2}{N}} \tag{E1}$$

where N is the number of atoms in the material. Note that in contrast to the definition of formation energy, here we use a root mean square difference between the compound and its elemental references. This was done in order to prevent changes in ELF from cancelling one another out as electron localization shifts away from some elements and towards others during compound formation. The formation ELF thus provides a quantitative measure of the degree to which the electron localization predicted by DFT for a material differs from that of the corresponding elements.

For example, $\Delta\mathrm{ELF}_f$ for the compound PtO_2 is calculated as

$$\Delta\mathrm{ELF}_{\mathrm{PtO_2}} = \sqrt{\frac{(\mathrm{ELF_{Pt,PtO_2}} - \mathrm{ELF_{Pt,el}})^2 + 2(\mathrm{ELF_{O,PtO_2}} - \mathrm{ELF_{O,el}})^2}{3}} \tag{E2}$$

A graphical example illustrating the ELF generated by r^{2}SCAN and SCAN for PtO_2 is shown in Figure E.1. In general, oxide compounds displayed larger changes in formation ELF from r^{2}SCAN and SCAN than other types of compounds, and PtO_2 exhibited a particularly large change in $\Delta\mathrm{ELF}_f$. As shown in the figure, local changes of $\pm 10\%$ occurred around the oxygen atoms in this material, resulting in $\Delta\mathrm{ELF}_f^{\mathrm{r^2SCAN}} = 0.03899$ and $\Delta\mathrm{ELF}_f^{\mathrm{SCAN}} = 0.00989$, and a change from SCAN to r^{2}SCAN of $+0.0291$, or a 294% increase over the SCAN value.

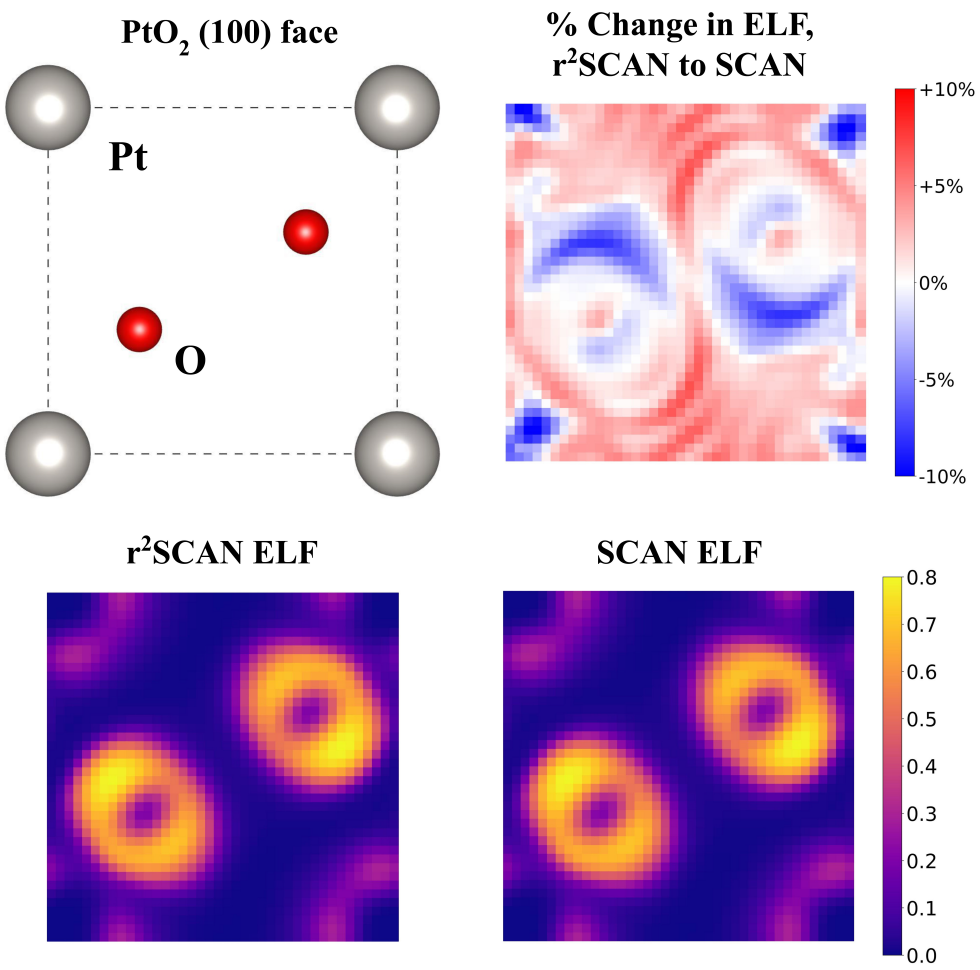

FIG. E.1. Illustration of shifts in electron localization (as described by the ELF) from r^{2}SCAN to SCAN as shown on the (100) face of PtO_2.

Appendix F: Electronic energy of r^{2}SCAN and SCAN elements

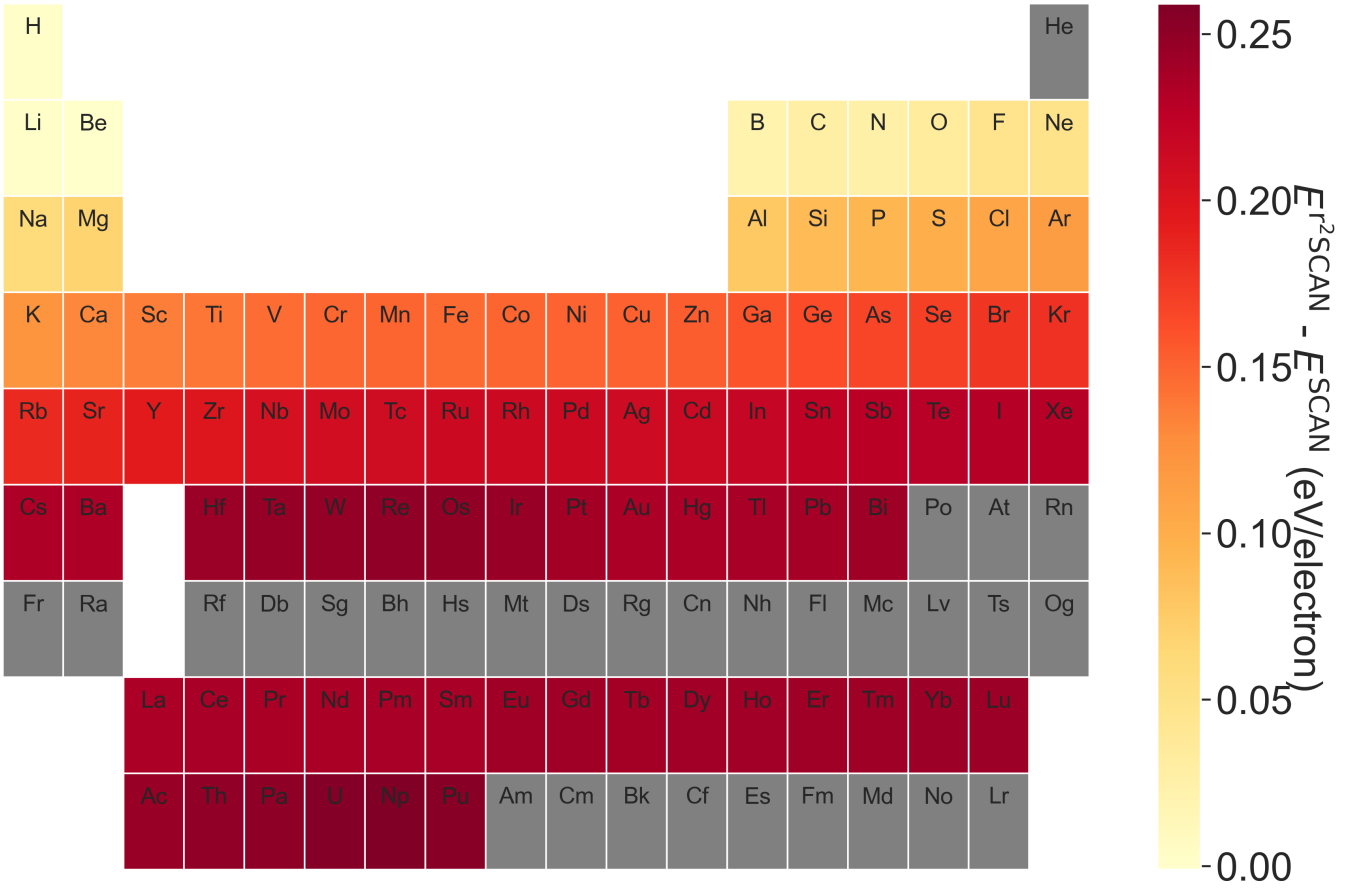

FIG. F.1. Difference in electronic energy (i.e., DFT energy) computed by r^{2}SCAN and SCAN for ground-state elements. The systematic trend with atomic number may be explained by considering that as the number of electrons increases, the amount of slowly-varying density (where $\alpha \approx 1$) increases, and these are the regions in which the different formulations of the gradient expansion terms in r^{2}SCAN and SCAN have the most effect [25, 49]. Note that in general, the electronic energies generated by DFT calculations using pseudopotentials do not have a clear physical interpretation. However, VASP uses all-electron potentials for the elements `H`, `He`, `Li`, and `Be` which makes the comparison of energies for those elements more physically meaningful [31].

Appendix G: Differences in r^{2}SCAN and SCAN formation energy by element

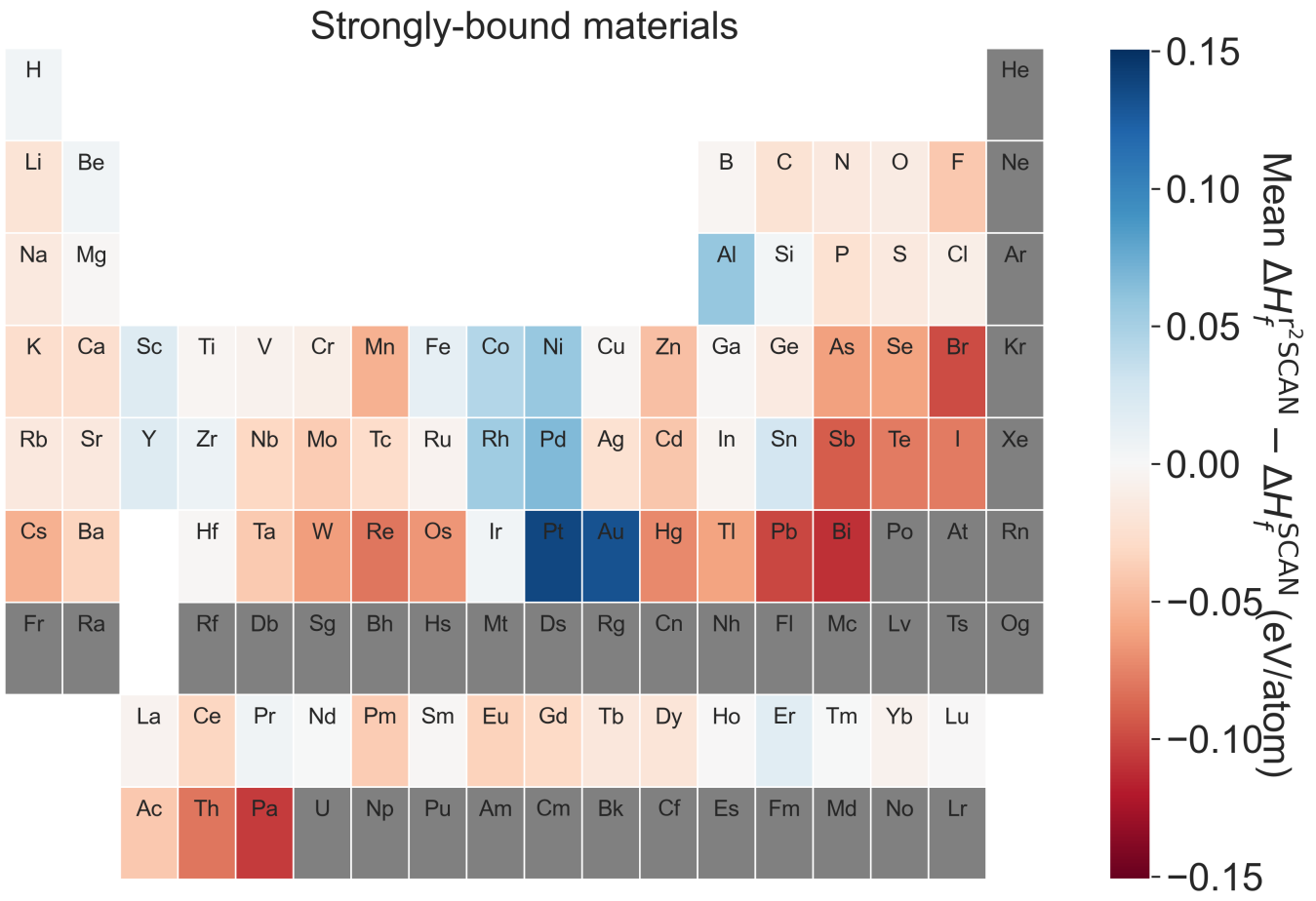

FIG. G.1. Differences in r^{2}SCAN and SCAN formation energy for strongly-bound materials. The periodic table is colored according to the average difference in ΔH_f per atom. The difference in ΔH_f is counted once for each element in a compound, and the values for each element are averaged. Hence, the compound `NpP`, for which $\Delta H_f^{\mathrm{r^2SCAN}} - \Delta H_f^{\mathrm{SCAN}} = -0.754$ eV/atom would contribute a value of -0.754 to both the Np and P boxes.

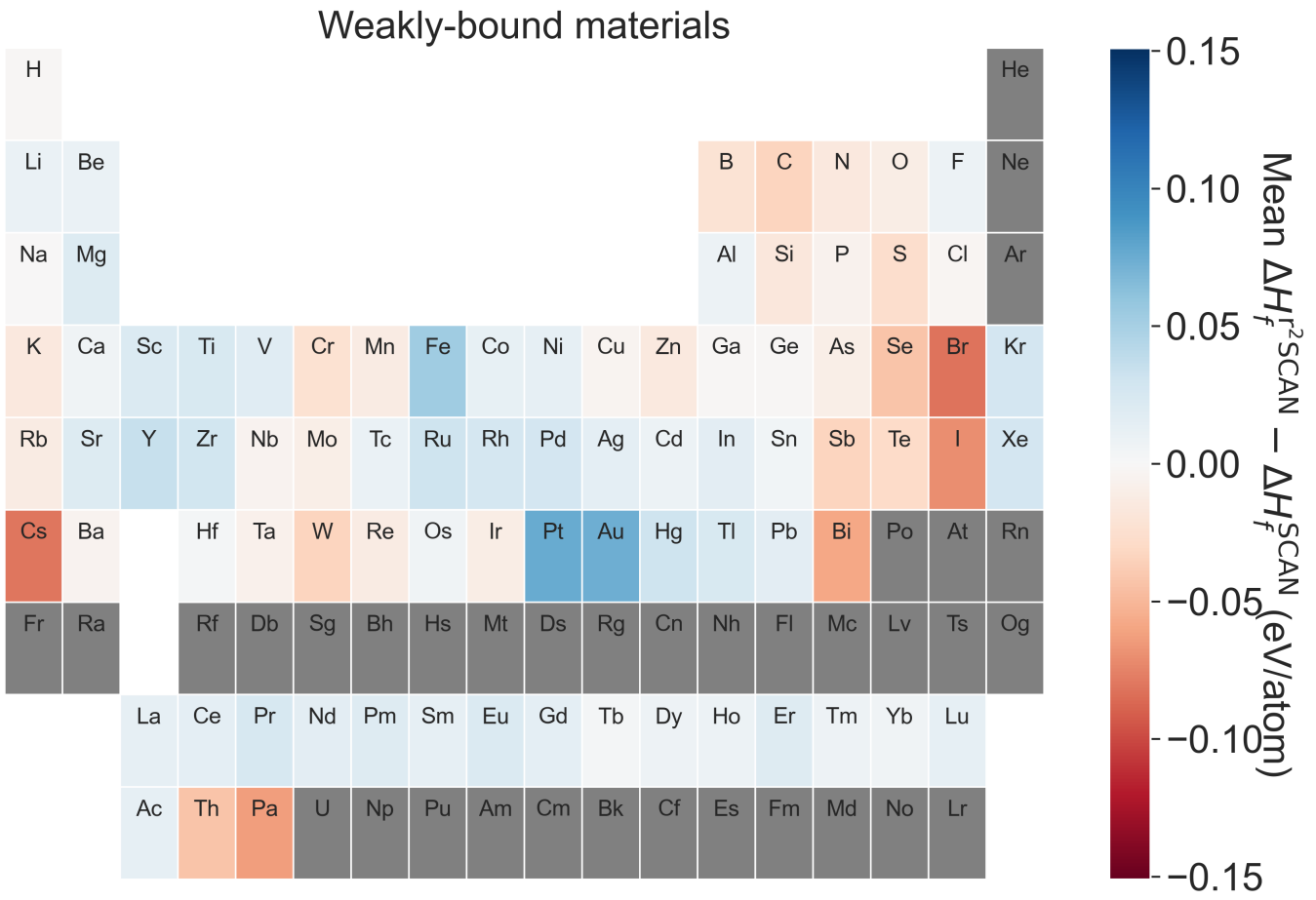

FIG. G.2. Differences in r^{2}SCAN and SCAN formation energy for weakly-bound materials. The periodic table is colored according to the average difference in ΔH_f per atom. The difference in ΔH_f is counted once for each element in a compound, and the values for each element are averaged. Hence, the compound `NpP`, for which $\Delta H_f^{\mathrm{r^2SCAN}} - \Delta H_f^{\mathrm{SCAN}} = -0.754$ eV/atom would contribute a value of -0.754 to both the Np and P boxes.

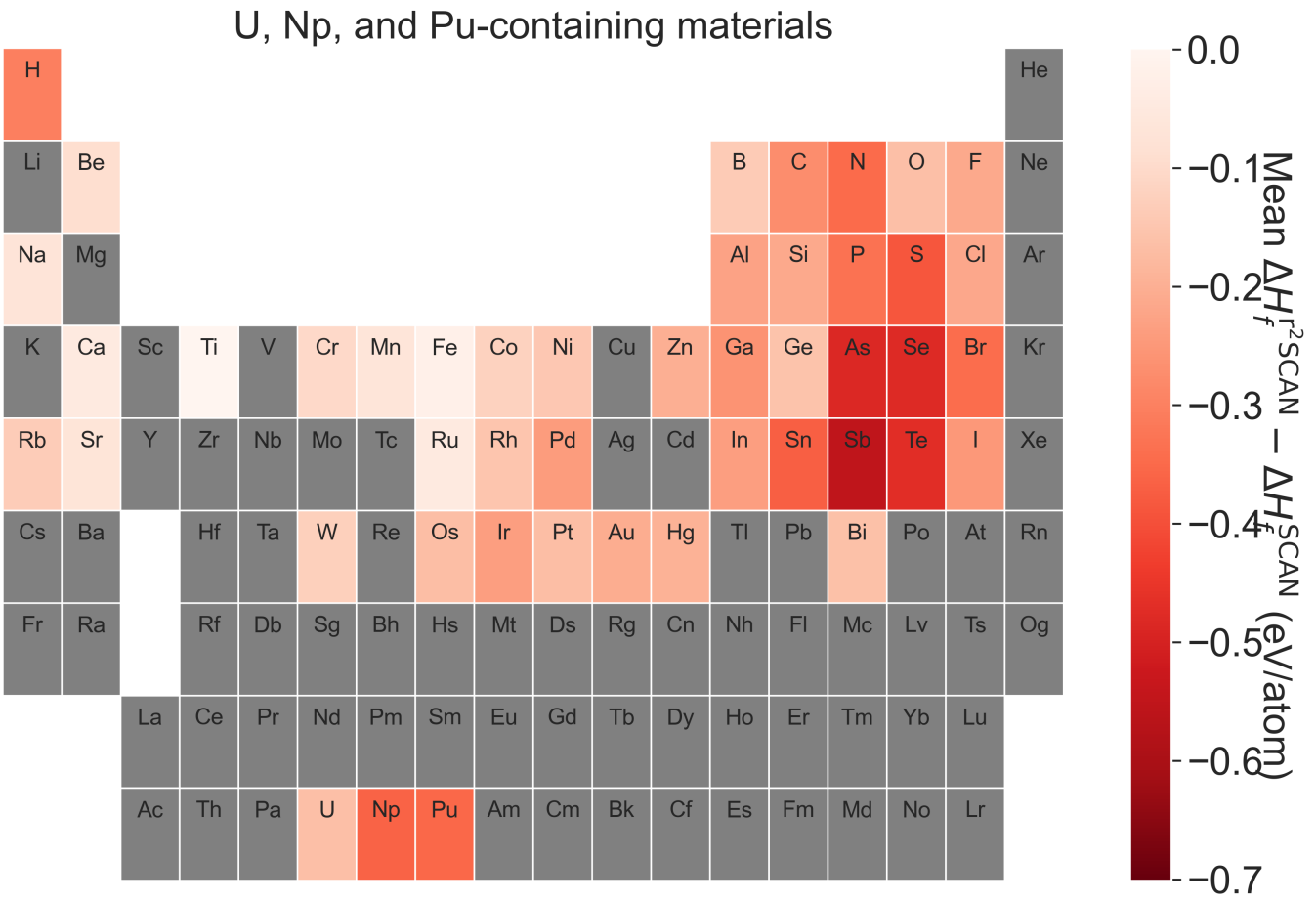

FIG. G.3. Differences in r^{2}SCAN and SCAN formation energy for `U`, `Np`, and `Pu`-containing materials. The periodic table is colored according to the average difference in ΔH_f per atom. The difference in ΔH_f is counted once for each element in a compound, and the values for each element are averaged. Hence, the compound `NpP`, for which $\Delta H_f^{\mathrm{r^2SCAN}} - \Delta H_f^{\mathrm{SCAN}} = -0.754$ eV/atom would contribute a value of -0.754 to both the Np and P boxes.

Appendix H: Experimental benchmarking data

Experimental formation enthalpy and bandgap data were obtained from the `expt_formation_enthalpy_kingsbury` and `expt_gap_kingsbury` datasets distributed with Matminer[50], respectively. The formation energy data comprise 2,135 unique materials and were compiled primarily from the Kubaschewski tables[51], the NIST JANAF database[52], and the compilation of Kim et al.[53, 54], as described in previous work [55]. 1,580 of these materials are associated with a specific Materials Project ID (mp-id) via the `likely_mpid` field. The bandgap dataset was derived from Zhuo et al.[56] and contains 4,604 materials, of which 2,481 have a `likely_mpid`. `likely_mpid` for the bandgap data were assigned using the same procedure used for the formation enthalpy data, which is described in previous work [55]. In this study, we match the mp-id of each computed material to the `likely_mpid` in the respective datasets to determine the corresponding experimental formation enthalpy and bandgap. Experimental lattice volumes were obtained from the Inorganic Crystal Structure Database (ICSD) [36]. Each `mpid` in the the Materials Project database has an associated set of ICSD identifiers that correspond to a single experimental entry in the ICSD. We calculated the median volume of all the ICSD structures associated with a material's `likely_mpid`, and report this as the experimental volume.

Appendix I: List of VASP pseudopotentials used

All calculations used pseudopotentials from the "PBE PAW datasets version 54" set released in September 2015. The table below lists the specific pseudopotential (i.e., `POTCAR`) used for each element. An up-to-date list of `POTCAR` symbols can always be found in the `MPScanRelaxSet` class in pymatgen [40].

Element	POTCAR Symbol
Ac	Ac
Ag	Ag
Al	Al
Ar	Ar
As	As
Au	Au
B	B
Ba	Ba_sv
Be	Be_sv
Bi	Bi
Br	Br
C	C
Ca	Ca_sv
Cd	Cd
Ce	Ce
Cl	Cl
Co	Co
Cr	Cr_pv
Cs	Cs_sv
Cu	Cu_pv
Dy	Dy_3
Er	Er_3
Eu	Eu
F	F
Fe	Fe_pv
Ga	Ga_d
Gd	Gd
Ge	Ge_d
H	H
He	He
Hf	Hf_pv
Hg	Hg
Ho	Ho_3
I	I
In	In_d
Ir	Ir
K	K_sv
Kr	Kr
La	La
Li	Li_sv
Lu	Lu_3
Mg	Mg_pv
Mn	Mn_pv
Mo	Mo_pv
N	N
Na	Na_pv
Nb	Nb_pv
Nd	Nd_3
Ne	Ne
Ni	Ni_pv
Np	Np
O	O
Os	Os_pv
P	P

Element	POTCAR Symbol
Pa	Pa
Pb	Pb_d
Pd	Pd
Pm	Pm_3
Pr	Pr_3
Pt	Pt
Pu	Pu
Rb	Rb_sv
Re	Re_pv
Rh	Rh_pv
Ru	Ru_pv
S	S
Sb	Sb
Sc	Sc_sv
Se	Se
Si	Si
Sm	Sm_3
Sn	Sn_d
Sr	Sr_sv
Ta	Ta_pv
Tb	Tb_3
Tc	Tc_pv
Te	Te
Th	Th
Ti	Ti_pv
Tl	Tl_d
Tm	Tm_3
U	U
V	V_pv
W	W_sv
Xe	Xe
Y	Y_sv
Yb	Yb_2
Zn	Zn
Zr	Zr_sv